GEOPHYSICS, VOL. 78, NO. 2 (MARCH-APRIL 2013); P. D93–D113, 22 FIGS., 5 TABLES.
10.1190/GEO2012-0388.1

Electric potential source localization reveals a borehole leak during hydraulic fracturing

A. K. Haas[1], A. Revil[2], M. Karaoulis[1], L. Frash[3], J. Hampton[3], M. Gutierrez[3], and M. Mooney[3]

ABSTRACT

A laboratory experiment was performed to see if passively recorded electric signals can be inverted to retrieve the position of fluid leakages along a well during an attempt to hydraulically fracture a porous block in the laboratory. The cubic block was instrumented with 32 nonpolarizing sintered Ag/AgCl electrodes. During the test, several events were detected corresponding to fluid leakoff along the seal of the well. Each event showed a quick burst in the electric field followed by an exponential-type relaxation of the potential distribution over time. The occurrence of these "electric" events was always correlated with a burst in the acoustic emissions and a change in the fluid pressure. These self-potential data were inverted in two steps: (1) using a deterministic least-square algorithm with focusing to retrieve the position of the source current density in the block for a given snapshot in the electric potential distribution and (2) using a genetic algorithm to refine the position of the source current density on a denser grid. The results of the inversion were found to be in excellent agreement with the position of the well where the hydraulic test was performed and with the localization of the acoustic emissions in the vicinity of this well. This experiment indicates that passively recorded electric signals can be used to monitor fluid flow along the well during leakages, and perhaps monitor fluid flow for numerous applications involving hydromechanical disturbances.

INTRODUCTION

Hydraulic fracturing has become a very important method to increase the permeability of shales and tight sandstones (Agarwal et al., 1979) and to increase the production of geothermal fields (Kohl et al., 1995). Hydraulic fracturing can also be used for the nonexempt solids waste disposal (Keck and Withers, 1979), in situ stress measurements (Kuriyagawa et al., 1989), and can occur during the grouting of the foundations of dams (Lee et al., 1999). The classical method for monitoring hydraulic fracturing remains acoustic emissions (microseismic), and significant progress has been made in the last decade in using passive seismic in detecting hydraulic fracturing events and localizing these events in heterogeneous materials. However, with acoustic emissions there is generally a lack of knowledge of where the fluids are actually moving within the subsurface formations as well as the actual extent of the fracture network (e.g., Warpinski, 1991). There is also a recognized need for methods that can be used to monitor fluid leakages around the walls of a borehole, which are also associated with the opening of fluid flow pathways in response to hydromechanical stimulations. This is particularly critical for boreholes that traverse through fresh-water aquifers where contamination is a concern (Cihan et al., 2011).

The self-potential method corresponds to the passive measurements of electric signals associated with a variety of source current mechanisms in the conductive subsurface of the earth including a redox-based contribution (Sato and Mooney, 1960; Castermant et al., 2008; Mendonça, 2008; Revil et al., 2010) and a streaming current contribution related to groundwater flow (Revil and Linde, 2006; Revil et al., 2011; Ikard et al., 2012). The self-potential inverse problem is similar in essence to electroencephalography (EEG) in medical imaging. In the last decade, the recording and inversion of EEG signals has been instrumental in our understanding of how the brain works and

Manuscript received by the Editor 17 September 2012; revised manuscript received 15 November 2012; published online 7 March 2013.
[1]Colorado School of Mines, Department of Geophysics, Golden, Colorado, USA. E-mail: mygeophysics@gmail.com; marios.karaoulis@gmail.com.
[2]Colorado School of Mines, Department of Geophysics, Golden, Colorado, USA and ISTerre, CNRS, UMR CNRS 5275, Université de Savoie, Le Bourget du Lac, France. E-mail: arevil@mines.edu.
[3]Colorado School of Mines, Department of Civil & Environmental Engineering, Golden, Colorado, USA. E-mail: lfrash@mymail.mines.edu; jesse.hampton05@gmail.com; mgutierr@mines.edu; mmooney@mines.edu.

in the mapping of its various functions (Grech et al., 2008; Duru et al., 2009).

The flow of pore water associated with hydraulic fracturing and leakages results in measurable voltages both during field operation in reservoir environments (Chen et al., 2005, 2007, 2011; Entov et al., 2010), in shallow aquifers (Wishart et al., 2008), or associated with artificial seismic sources (Kuznetsov et al., 2001). Similar conclusions have been reached in volcanic environments (e.g., Byrdina et al., 2003) and there is a relatively broad base of literature on laboratory observations of electromagnetic fields associated with hydromechanical disturbances (Moore and Glaser, 2007; Jia et al., 2009; Nie et al., 2009; Chen and Wang, 2011; He et al., 2011, 2012; Onuma et al., 2011; Wang et al., 2011).

For instance, Moore and Glaser (2007) investigate unconfined and confined samples of granite subjected to hydraulic fracturing in the laboratory. Their results indicate that the principal mechanism for the self-potential response is due to the generation of a streaming source current density associated with the flow of the pore water (see Wurmstich and Morgan, 1994; Ushijima et al., 1999). We believe that these voltages carry information about the fracture network that is expected to be complementary to the information determined from microseismic, tiltmeter, wellhead pressure, and wellhead flow measurements (Keck and Withers, 1979). Mahardika et al. (2012) recently provided a comprehensive framework to perform full-waveform inversion of both passive seismic and electric data to invert for the position and moment tensor of hydromechanical events.

In the present study, we are concerned with the time-lapse monitoring of a hydraulic fracturing/leak-off experiment in the laboratory using the time-lapse record of self-potential signals. Our goal is to show that the inversion of electric potential measurements can be used to detect and localize the streaming current disturbances caused by borehole seal failure and the resulting undesirable fluid migration along the borehole during hydraulic fracturing operations. A leak-off resulted from an attempt to hydraulically fracture a porous block and our initial goal was to study the electric signals associated with such fracturing event. That said, the rupture of the seal was responsible for several bursts of acoustic emissions that will be analyzed as well.

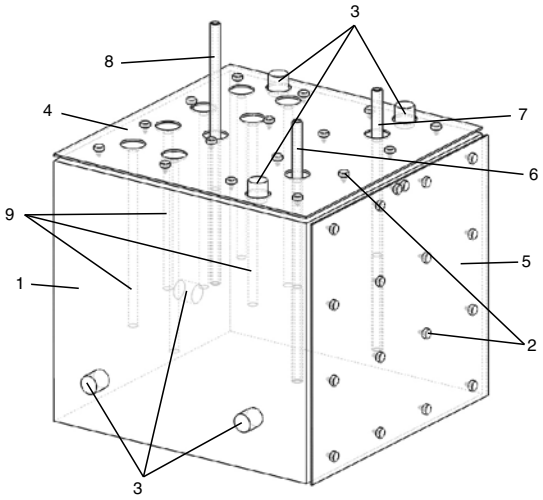

Figure 1. Unconfined cement block sensor configuration. (1) Cement block (2) 34 Ag/AgCl electrodes (Biosemi) (3) acoustic emission sensors (Mistras WSα) (4) plastic plate with top array of 16 channels of Ag/AgCl electrodes (Biosemi) (5) plastic plate with back array of 16 channels of Ag/AgCl electrodes (Biosemi) (6) hole #9 high-pressure fluid-injection tube (7) hole 10, high-pressure fluid-injection tube (8) hole 6, high-pressure fluid-injection tube (not used), and (9) other holes (no injection).

MATERIAL AND METHOD

Equipment

The porous material used for the laboratory fracturing tests is a cement mixture (FastSet Grout Mix). It was cured for about 10 months before the tests proceeded. The porous sample has a cubical shape ($x = 30.5$ cm $\times$ $y = 30.5$ cm $\times$ $z = 27.5$ cm, Figure 1). After curing, several 10-mm diameter holes (named #1 to #10 below) were drilled into the block to varying depths such that various tube sealing methods could be tested (see Figure 1). Stainless steel tubing with a 9.5-mm outside diameter was placed into a few holes using Loctite Instant Mix 5-Minute epoxy as the tube sealing agent. The voltage measurement electrodes were attached to the top and one side of the block (16 electrodes on each face) using a plastic template for precise positioning. Six acoustic emission sensors were also mounted to three faces of the block. The electrodes were solid sintered Ag grains with a solid AgCl coating. The active diameter of the electrodes was about 1 mm. Each electrode has a voltage amplifier built into the electrode casing. Each of these electrodes was electrically connected to the block surface through a drop of conductive gel usually used for EEG.

The electric response during the experiment was measured using a very sensitive multichannel voltmeter manufactured by Biosemi, Inc., designed for EEG (http://www.biosemi.com/). In the experiments, the electric potential measurements were acquired with 32 amplified nonpolarizing silver-silver chloride (Ag AgCl) electrodes. The electrode potentials were measured using the BioSemi ActiveTwo data acquisition system that is self-contained, battery powered, galvanically isolated, and digitally multiplexed with a single high-sensitivity analog-to-digital converter per measurement channel. The analog-to-digital converters used in the system were based on a Sigma-Delta architecture with a 24-bit resolution. The system has a typical sampling rate of 2048 Hz with an overall response of DC to 400 Hz. This measurement system has a scaled quantization level of 31.25 nV (least significant bit, or "LSB") with 0.8 μV rms noise at a full bandwidth of 400 Hz with a specified $1/f$ noise of 1 μV pk-pk from 0.1 to 10 Hz. The common mode rejection ratio was higher than 100 dB at 50 Hz, and the amplified nonpolarizing electrode input impedance was 300 MΩ at 50 Hz (10^{12} ohm//11 pF) (see http://www.biosemi.com/; Crespy et al. [2008] and Ikard et al. [2012] for further explanations).

The voltage reference for the measurements is contained within the measurement area, and was designed into the measurement system to be a part of the common mode sense (CMS) and common mode range control (DRL) electrodes (see Ansari-Asl et al. [2007] for further information on the common mode control used in the BioSemi System and Kappenman and Luck [2010] for the effect of electrode impedance on the measured response). The CMS and DRL electrodes used in combination to make a feedback control system that keeps the CMS electrode as close as possible to the reference voltage at the analog to digital converter. In this system, the CMS electrode becomes a dynamic reference potential. All of the digitized data are saved in the raw data form, and is referenced to the CMS electrode. The data are recorded with all of the common

mode signals and, as a result, any channel can be used as the reference channel. In fact, the maximum common mode rejection in the system only fully occurs when a single channel of choice is subtracted from all of the other channels. In our measurements we selected the least active signal in the data (channel 4) as the reference. This type of system allows us to change the reference electrode as needed to correct for dynamic voltages occurring at the CMS electrode. Therefore, this type of system is best suited for dynamic self-potential signals. The entire system, including the computer, is operated on batteries to minimize conductive coupling with the electric power system. The flow chart used to analyze the raw electric data is shown in Figure 2.

Acoustic emissions were also monitored using six WSα sensors manufactured by Physical Acoustics Corporation (PAC, see position in Figure 1). All six sensors had an operational frequency of 100–900 kHz and a resonant frequency of 125 kHz. PAC's Micro-II PCI-2-8 Digital Acoustic Emission (AE) System chassis was used to run AEwin data collection and posttest data analysis software. The Micro-II chassis performs at a 40-MHz acquisition with sample averaging and automatic offset control. Waveform streaming enables data acquisition to hard disk continuously with up to 10 MHz. PAC's 2/4/6 (20/40/60 dB gain) single-ended preamplifiers were used on each channel throughout all testing. A 60-dB gain setting was preferred to amplify microfracture signals and increase signal-to-noise ratios (S/Ns). The acoustic emission data were also inverted to localize the position of the source (see Hampton [2012] for additional details).

Experiment

The experiments were conducted on the porous block in equilibrium with the atmosphere of the laboratory (~30% relative humidity). Saline water was used as the injection or fracturing fluid (no sand, or other particles were used to prop open fractures) containing 10 g of NaCl dissolved into 1000 ml of deionized water (conductivity of 1.76 S m^{-1} at 25°C). Note: because lower salinities imply higher electrokinetic signals, we place ourselves in the most difficult conditions we could meet in the field. We demonstrate below that even in such high salinity conditions, the self-potential signals can be easily observed. The fluid control system injects fluid through stainless steel tubes (Figure 1) using a computer controlled Teledyne Isco 100DX syringe pump that is able to control flow rate or pressure. The injection tube was designed to have an open end at the bottom; there were no side ports for fluid to flow through. The system has a total fluid capacity of 103 ml, and is capable of achieving pressures up to 68.9 MPa and maintaining constant flow rates of 0.001 to 60 ml/ min. In this experiment, the injection tubes were initially pressurized to a proportional-integral-derivative controlled 1.17 kPa with the fracturing fluid and maintained at that pressure for a period of time to be sure that the system was maintaining pressure and to measure the fluid flow rate. A constant fluid flow rate of 1 ml/ min was then imposed on the system with the intent of inducing hydraulic fracturing. Under constant flow, the cement block or the tubing seal would eventually fail.

The test procedure began by preparing the cement block for high pressure injection (see Frash and Gutierrez [2012] for details). The

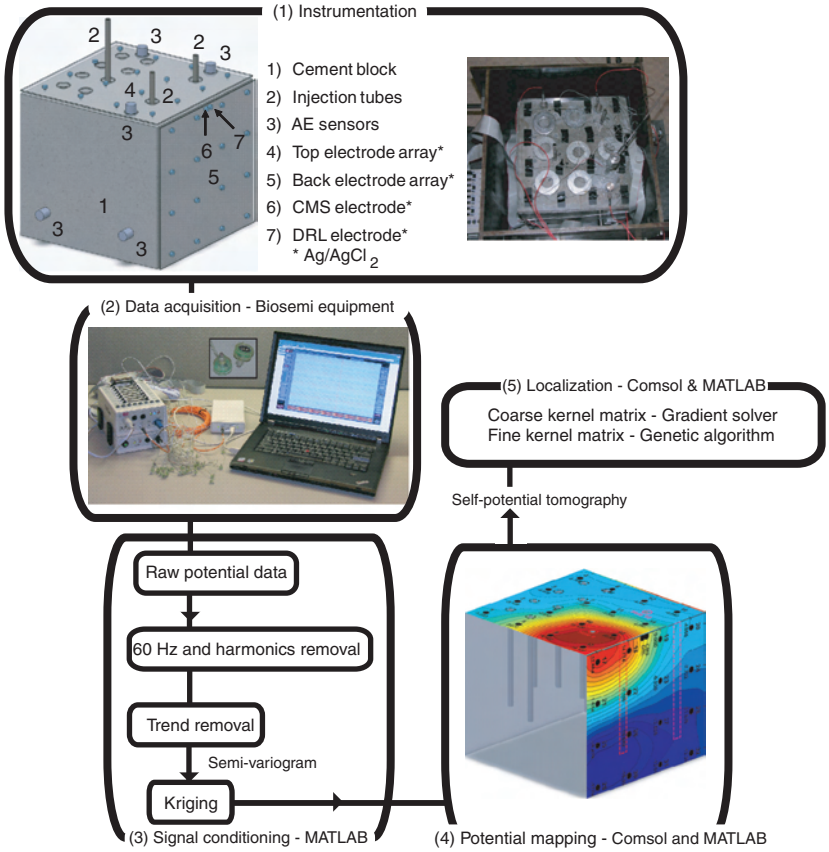

Figure 2. Flow chart for the processing of the electric potential data. (1) Instrumentation of the porous block. (2) Data acquisition showing the BioSemi EEG system and the laptop computer. (3) Signal condition of the raw data. (4) Mapping the voltage response using ordinary kriging. (5) Localization of the causative sources in the block.

injector was filled with the saline solution described above and coupled to the injection tube that was also filled with the saline solution. The injection system was purged of air, and then subjected to constant pressure of 1.17 kPa for about 30 min to monitor leak-off to be sure that there was no pressure loss. For the experiment associated with hole #9, a 60-s preinjection (termed phase 0) electric potential measurement period was acquired (Figure 3a). The goal of this phase was to establish individual channel offsets and drift trends for use during post acquisition signal processing. Constant pressure fluid injection at 1.17 kPa (termed phase 1) was initiated at T0 = 60 s and terminated at T1 = 1632 s. This phase was followed by phase 2, a 1-ml/min constant flow rate initiated at T2 = 1795 s (note that fluid pressure was maintained, but not actively controlled between T1 and T2). Fluid injection was terminated well after the end of the electric data acquisition, when seal failure was confirmed through the appearance of water on the surface of the block near the injection well. For this experiment, self-potential data acquisition terminated at 2086 s, prior to completion of phase 2 injection due to an accidental interruption of the streaming data because of a poor USB 2.0 connection. This did not affect the raw data saved or any subsequent use of the data.

OBSERVATIONS

Electric potential data

Figure 3 shows the temporal evolution of the electric potential for all of the electrodes, including the occurrence of bursts in the electric potential that are similar in shape (but much larger in amplitude) to the electric-field bursts observed by Haas and Revil (2009) for Haines jumps during the drainage of an initially water-saturated sandbox. Figure 3a shows the entire 2086 s record, while Figure 3b, 3c, and 3d zooms in on specific areas of interest. There are seven major events of which three are highlighted (events E1 through E3), and two will be used below to test our localization procedure. These events are shown in the time series of Figure 3b, 3c, and 3d. All major electric potential events occurred during phase 2 constant flow injection. During phase 1, the measured electric potential gradually increases as fluid is being injected into the cement block. No bursts in the electric field were observed during the constant pressure phase (phase 1).

Each major event is characterized by a rapid change in the electric potential time series followed by a slower exponential-type

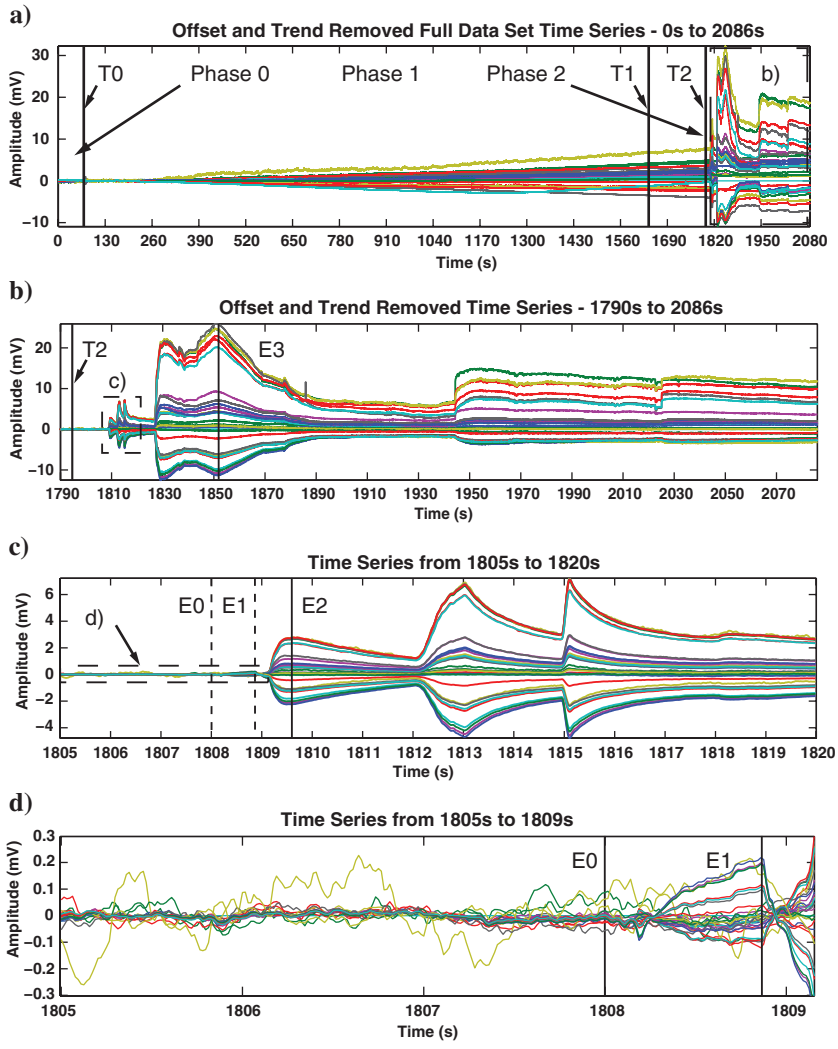

Figure 3. Self-potential time series related to hole #9 saline water injection. (a) Full time series data set showing the different fluid injection time periods during data acquisition (T0, T1, and T2). Note the significant change in electric response after T2 that is bounded by region (b). (b) Zoom highlighting the background normalized electric response showing distinct electric impulses related to the start of constant flow injection at T2 with the selected E3 event. (c) Zoom in region (c) highlighting the first series of impulsive signals with selected peak event E2 with temporal reference to E0 and E1. (d) Zoom in region (d) showing the temporal noise leading up to event E1, with a voltage background time slice at E0. Note the change in potential after E1.

relaxation of the potential with a characteristic time comprising between several seconds to several tens of seconds. This relaxation is believed to be associated with the relaxation of the fluid pressure as shown later. Because the relaxation of the potential distribution is relatively slow after each event, a sequence of overlapping events causes a superposition of the potentials from each event in the sequence to varying degrees (see Figure 3b and 3c). We term the superposition of a past event decay response with a new event a residual potential superposition. It can be clearly seen from Figure 3 that the degree of residual potential superposition is dependent on event physics (hydroelectric coupling), event magnitudes, event spatial distribution, time of occurrence, and event decay rate. Each of these factors is variable, and to localize and characterize individual impulsive events, the influence of residual potential superposition must be accounted for, and removed to complete a comprehensive analysis of the data.

Figures 4 and 5 show the spatial evolution of the electric potential on the monitored faces of the test block, starting with snapshot #E0 taken prior the occurrence of events E1 and E3. For these snapshots, ordinary spatial kriging was performed on each face separately. It can be seen in Figures 3d, 4a, and 4b that the snapshot E0 shows random spatial electric-potential fluctuations associated with the temporal noise that can be seen in Figure 3d. In these figures, channel 13 is noisier with respect to the rest of the channels possibly from poor contact between the electrode and the cement block.

Event E1 in Figure 4c and 4d shows an initial voltage distribution with a small negative potential on the top surface of the block and a bipolar signal on the side of the block. This voltage distribution implies that there is a current source density possibly near hole #9 (see position in Figure 1) that is pointing mostly downward into the block. The time series in Figure 3d shows the onset of this small peak (event E1), followed by a quick decay and reversal of the polarity of the current source density as indicated by event E2 as shown in Figures 3c, 5a, and 5b. We consider that the polarity reversal may be described by a sequence of events. First, a brief pressure drop (E1p), seen in Figure 6 just before the E1 peak, indicates some sort of pulse flow of fluid occurred that may have led up to the E1 peak. The following reversal of polarity that peaks at E2 is correlated with another pressure drop (Figure 6, E2p) just prior to the peak at E2. This indicates that the initial fluid flow direction at E1 was in a downward direction, possibly an indication of the initial downward direction of a plastic failure in the epoxy seal before the reversal of flow direction due to other seal failures with higher volumes and mostly vertical flow directions. It is possible that the impulsive nature of these failures was unique to this particular epoxy seal technique that caused plastic seal failure. Additionally, gas pockets inside the epoxy interface with the hole wall could be an explanation of the burst nature of the seal failure. This could have been caused by unequal distribution of the epoxy along the hole wall. The rupture of each gas pocket would produce a drop in pressure followed by an increase in the fluid flow along the hole wall, and an electrokinetic response. As we will show later, the direction of the current density corresponding to event E2 is mostly pointing upward and grows in magnitude in an impulsive manner as the fluid injection proceeds. The magnitude of the electric potential grows from event E2 onward, and maintains the spatial voltage distribution/polarity throughout the remainder of the data acquisition. This implies that fluid is moving upward in a persistent manner, somewhere in the vicinity of hole #9 during and after event E2.

Pressure and acoustic emission data

The hole #9 fluid pressure change (sampled at 5 Hz) response during constant flow injection (phase 2) is shown in Figure 6 along with the acoustic emission hit count versus time histogram that is shown in Figure 6a. The acoustic emission hit counts peak very close to and during the pressure changes. This indicates some sort

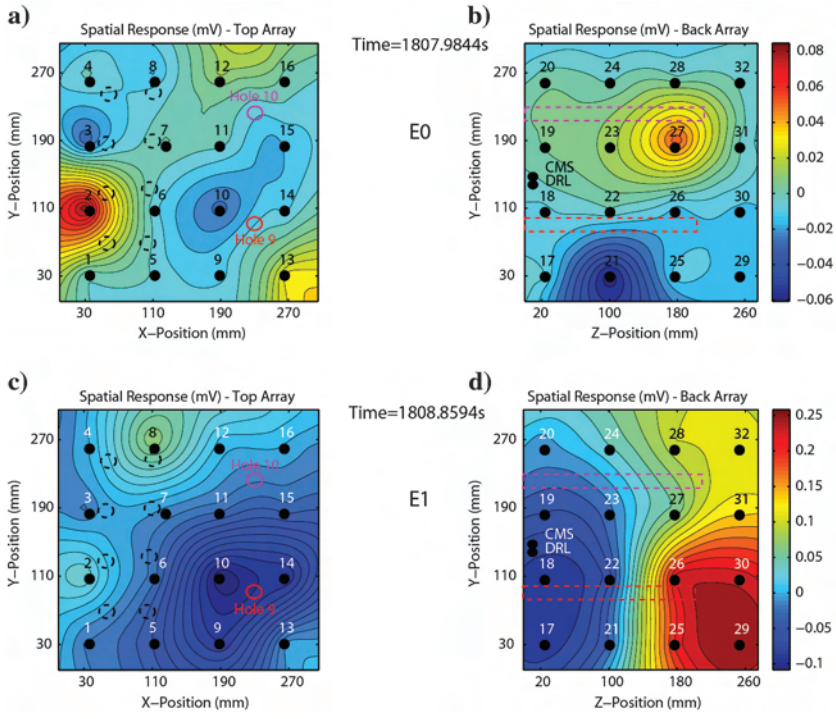

Figure 4. Self-potential spatial voltage distributions for the snapshot E0 and the event E1. Each panel is a kriged contoured distribution of the electric potential on the top and back panels (ordinary kriging). The black dots denote the position of the electrode positions, the dashed circles represent the positions and sizes of other holes within the test block, and the dashed lines represent projections of the positions and depths of hole #9 and hole #10 onto the back face of the block (present in all spatial voltage distribution figures). (a and b) Spatial electric potential distribution for snapshot E0 showing the spatial variations associated with the background noise. Note the very small color bar voltage scale (+0.08 mV to −0.06 mV). (c and d) Voltage distribution for event E1 showing the burst of the electric field associated with the first hydraulic pulse taking place during constant flow injection. Note the voltage polarities in the spatial distributions and the much larger color bar voltage scale (+0.25 mV to −0.1 mV).

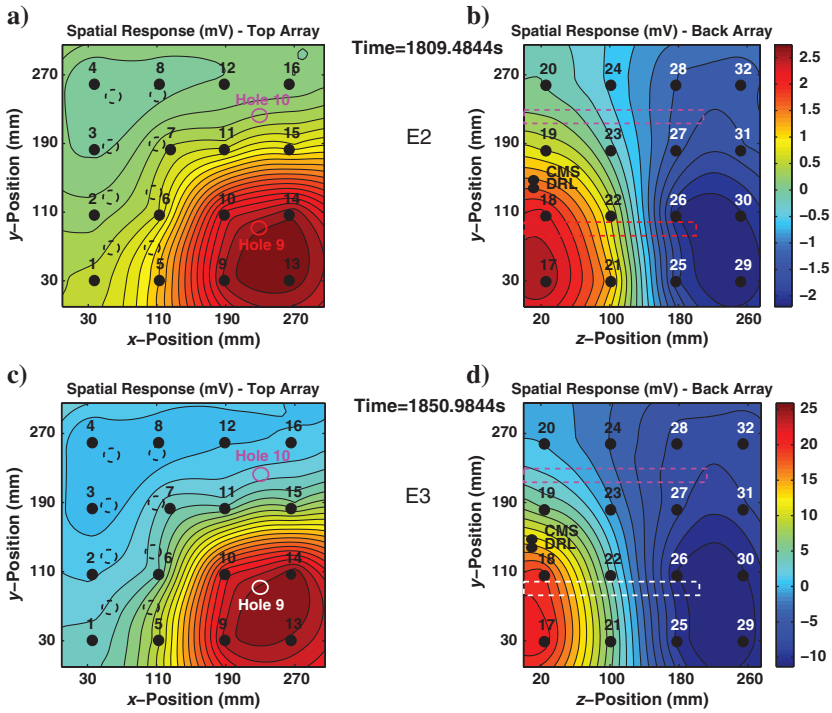

Figure 5. Self-potential spatial voltage distributions of events E2 and E3. (a and b) Event E2 voltage distribution showing the peak voltage associated with the second hydraulic pulse during constant flow injection. Note the voltage polarities in the spatial distributions and the color bar voltage scale (+2.5 mV to −2.0 mV). Event E2 represents the first of a series of electric field bursts. Panels (a and b) show a reversal in polarity and increase in peak magnitude relative to Figure 4 panels (c and d). (c and d) Event E3 spatial voltage distribution showing the peak voltage associated with the highest magnitude pulse during constant flow injection.

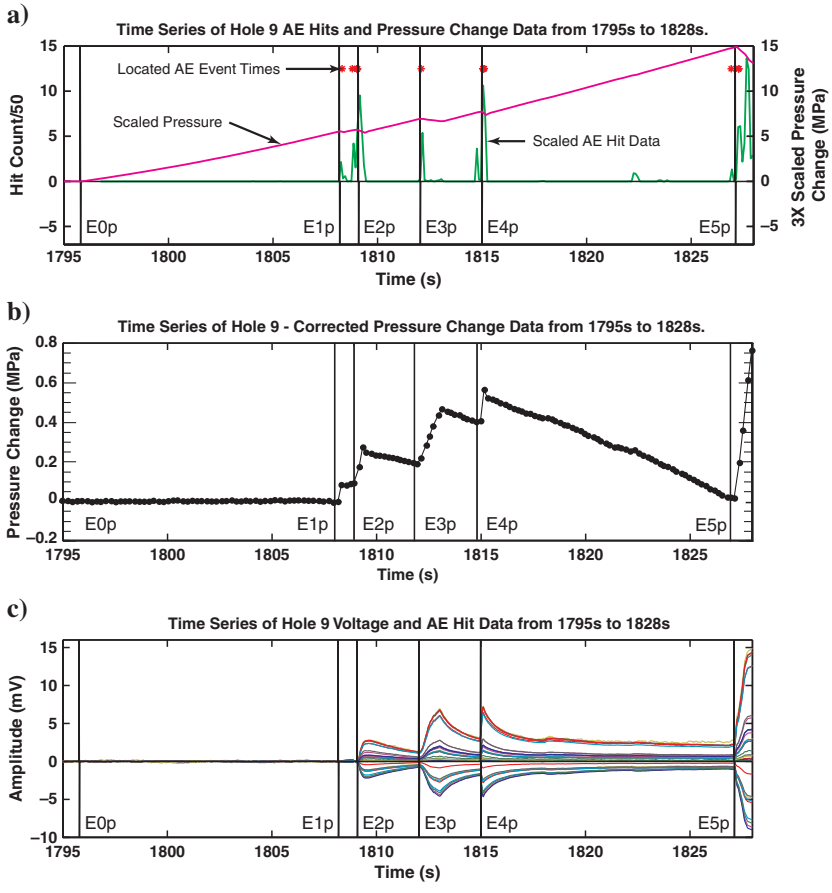

Figure 6. Fluid pressure, acoustic emissions, and electric potential changes during a given time window. (a) The acoustic emission (AE) data and pressure change correlation. The red asterisks denote the located acoustic emission events. (b) The trend removed pressure changes. (c) The voltage responses at all 32 measurement points. The events labeled E0p–E5p represent the same events in each panel of the figure. The acoustic emission hits, the pressure changes, and the voltage data all align, indicating that there is a relationship between these phenomena.

of breakage is occurring resulting in a momentary pressure drop during these times. The sequence is highly temporally correlated, and indicates breakage followed by periods of low acoustic emission activity. The acoustic emission hit counts close to event E1p, peak at 108 hits; the E2p count peaks at 477 hits; the E3p event peaks at 270 hits; the E4p hit count peaks at 532 hits, and the hit count at E5p is complex having three peaks, with a maximum count above 680 hits. The hits are based on exceeding an acoustic emission threshold level on each channel in the acoustic emission detection system. Only a few of the hits contain enough S/N, and channel-to-channel correlation without overlap to allow hit localization. If hits are localized, then they turn into acoustic emission events. Figure 6a also shows the temporal correlation of the located acoustic emission events. Figure 6b shows the trend removed pressure change data along with the event correlations, and Figure 6c shows the voltage response and pressure change event correlations.

Figure 6 shows that the observed bursts in the electric field are directly related to pressure changes that were measured in the injection system and acoustic emission hits. The pressure data indicate that there were some sharp changes in the flow regime inside hole #9 and the leakages were only occurring inside the block (the occurrence of electric data shows that the fluid that moved was in contact with porous media; no electrokinetic phenomena would occur outside the block and directly in the hole). The large number of temporally correlated acoustic emission hits indicate that something was breaking at the times of the pressure and voltage changes.

Note that the pressure data shows only small pressure fluctuations in the early phases of the seal failure around hole #9 while the pressure continues to build. The drops in pressure and correlated increases in voltage indicate that fluid is moving in the system. The drops in pressure indicate that the fluid flow rate through the seal failure is momentarily higher than the fluid flowing into the system. This higher fluid flow rate depletes the fluid volume and pressure in the fluid injection system until the pathway associated with the seal failure closes. Flat pressure response during seal failure may be expected if the seal failure were to achieve a state of equilibrium over a short period of time, and that the volume of flow into the system was equal to the volume of flow out of the system. This is clearly not the case here as we are dealing with a highly dynamic hydromechanical system.

If pressure measurements were the only observations of these events, then these fluctuations could not be directly attributed to a seal failure mechanism. However, the existence of electric data and acoustic emissions shows that there is a mechanism other than induced block fracturing going on. The electric data provides an information related to the flow process during the series of events in progress. The electric data implies seal failure, and the pressure data confirms fluid movement. The electric data actually provides more detail of the early development of the seal failure process and we will show that the electric field can be used to localize these events indicating an imminent seal failure. Each of the pressure drops shown in Figure 6 indicates that the seal is progressively failing (not full failure for each event), resulting in the burst like behavior described in the previous section. Only when the pressure decreases precipitously (E5p in Figure 6) can full seal failure be identified from the pressure data.

This combination of observations shows the strong correlation between mechanical effects and electric responses, indicating the breakage of material along with the movement of fluid in the system. Each observation by itself is insufficient to explain the physical processes occurring within the block; however, the combination of the measurements strengthens the understanding of the physical changes within the block.

Electric potential evidence of seal failure

The persistent voltage distribution shown in Figure 5 indicates the effects of upward fluid migration somewhere near hole #9. We believe that this set of observations provides a leading indicator of the borehole seal failure. This seal failure was further confirmed through fluid pressure measurements (see previous subsection) and the leakage along the borehole was later visually confirmed through the observation of water flow at the top surface of the block in the vicinity of hole #9. The temporal electric signatures in Figure 3 shows numerous impulsive events that grow as the seal failure progresses. The hypothesis for the explanation of these data considers that the epoxy seal failed in a plastic manner beginning with the onset of seal failure with subsequent repeated blockage and breakthrough events having a valve like behavior until the end of the data acquisition. The seal failure occurs in the epoxy-filled annulus of the borehole between the steel tube and the cement; as more fluid contacts the cement walls of the borehole with higher and higher velocities, the magnitude of the electric response grows accordingly. The approximate position of the fluid contact with the borehole wall can be determined from the data. Note that the position of the positive anomaly recorded by the top array is not centered on hole #9, but is displaced, from the center of the hole, possibly because of the position of the electrodes and the electric boundary conditions around the borehole.

The data from the side face electric potential array also contain source location and orientation information, indicating that the fluid flow encountered porous media somewhere well above the bottom of the borehole, also a potential indication of borehole seal failure. The observations imply that the fluid flow is occurring along a pathway following the borehole and close to the lower right corner of the top array. The electric boundary conditions in the borehole is insulating between the borehole wall and the stainless steel tubing, causing the reflection of the electric potential away from the borehole center. These electric potential measurements are consistent with the subsequent observations of fluid leakage at the test block surface near hole #9 due to borehole seal failure. These electric observations occurred several minutes before surface fluid leakage was visually observed on the top surface.

SOURCE LOCALIZATION ALGORITHMS

Our goal in this section is to apply a dipole-based inversion algorithm to localize the source of the electric disturbances in the block for the various events discussed above. We start by specifying the physical problem for the occurrence of the quasi-static electric potential distribution. Then we develop our inversion as follows: (1) We apply a gradient-based inversion with reduction of the volume of the source (compactness) followed by (2) a genetic algorithm localization to refine the position of the source.

Field equations

The coupling between the hydromechanical equations and the electromagnetic equations is described in Mahardika et al. (2012) including dynamic terms. The governing equation for the occurrence of self-potential signals is obtained by combining a

constitutive equation with a continuity equation. The constitutive equation corresponds to a generalized Ohm's law for the total current density $\mathbf{j}$ (in $\mathrm{A\,m^{-2}}$),

$$\mathbf{j} = \sigma\mathbf{E} + \mathbf{j}_S, \tag{1}$$

where σ denotes the low-frequency electric conductivity of the porous material (in $\mathrm{S\,m^{-1}}$), $\mathbf{E} = -\nabla\varphi$ the electric field in the quasi-static limit of the Maxwell equations (in $\mathrm{V\,m^{-1}}$), φ the electric potential (in V). The source current density is given by $\mathbf{j}_S = \hat{Q}_V\mathbf{u}$ where $\mathbf{u}$ denotes the darcy velocity and $\hat{Q}_V$ the excess of charge (of the diffuse layer) per unit pore volume of the porous or fractured material (in $\mathrm{C\,m^{-3}}$) that can be dragged by the flow of the pore water. At high flow rates, the flow can be influenced by the value of the Reynolds number; the case of high Reynolds numbers is analyzed by Bolève et al. (2007). Equation 1 can be combined with the following conservation equation for the charge in the quasi-static limit of the Maxwell equations:

$$\nabla \cdot \mathbf{j} = 0. \tag{2}$$

Combining equations 1 and 2 yields a Poisson's equation for the self-potential φ (expressed in V),

$$\nabla \cdot (\sigma\nabla\varphi) = \Im, \tag{3}$$

where $\Im$ denotes the volumetric current density (in $\mathrm{A\,m^{-3}}$). This volumetric current density is given by,

$$\Im \equiv \nabla \cdot \mathbf{j}_S = \hat{Q}_V\nabla \cdot \mathbf{u} + \nabla\hat{Q}_V \cdot \mathbf{u}. \tag{4}$$

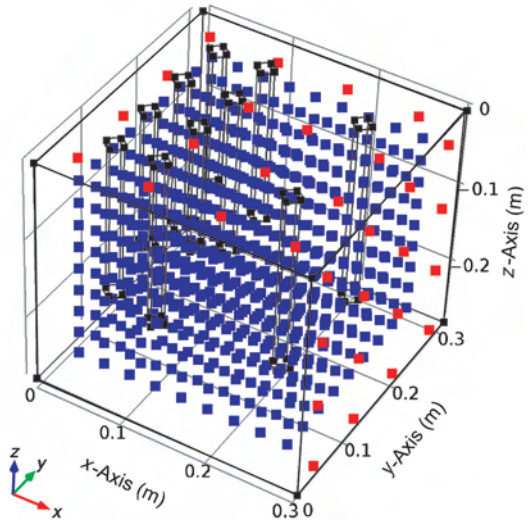

Figure 7. Comsol model showing the distribution of points used to compute the coarse kernel matrix (blue points, 729 positions) and the voltage measurement points (red points, 32 positions). The model geometry includes each of the 10 holes that were drilled into the block (black cylinders) considered to be perfect insulators. The arrows labeled x, y, and z indicate the positive directions of the corresponding axes in the figure for the Cartesian coordinate system.

The electric potential distribution at an observation point P is given by

$$\varphi(P) = \frac{1}{2\pi}\int_\Omega \rho\frac{\nabla \cdot \mathbf{j}_S(M)}{x(P,M)}dV + \frac{1}{2\pi}\int_\Omega \nabla\ \ln\ \rho(M) \cdot \frac{\mathbf{E}(M)}{x(P,M)}dV, \tag{5}$$

where x denotes the distance from the source at position M to the electrode located at position P where the electric potential signal is recorded. In equation 5, the two contributions associated with the primary field (first term of the right-hand side of equation 5 and the secondary potential (the second term of the right-hand side of equation 5 are separated. The primary source term is due to the hydro-mechanical disturbances, whereas the second term is due to the heterogeneities in the resistivity distribution of the resistive block.

Another possibility is to write the solution in a more compact form as

$$\varphi(P) = \int_\Omega \mathbf{K}(P,M)\mathbf{j}_S(M)dV, \tag{6}$$

where $\mathbf{K}(P, M)$ is called the kernel or the leading field and dV is a small volume around the source point M. We use this equation in the computations below in our attempt to localize the causative source of the electric bursts. Generally, the elements of the kernel are the Green functions connecting the self-potential data at a set of measurement stations P located at the measurement surface and the sources of current density at a set of source points located in the conducting volume. The kernel computation accounts for the electric resistivity distribution and the boundary conditions applied to the system. In the following computations, we will use a uniform resistivity distribution within the domain volume, not including the holes drilled into the block. Indeed, these holes represent infinite impedance zones within the volumetric resistivity distribution, and are explicitly accounted for in the computation of the kernel. Accounting for the presence of the holes within the volume is crucial to properly compute the kernel and localize the source current density. Figure 7 shows the 729 positions used for the computation of the kernel in the block.

Inversion phase 1: Gradient-based deterministic approach

Equation 6 can be written in the following matrix form,

$$\mathbf{d} = \mathbf{Km}, \tag{7}$$

where $\mathbf{d}$ denotes the N-vector of the observed electric potentials, at each time step, at N electrodes, The vector $\mathbf{m}$ is a $(3M)$-vector containing the M source current density terms (times three because we are dealing with a vector in a 3D cartesian coordinate system, having x, y, and z components), $\mathbf{K}$ denotes the kernel matrix.

The inverse problem is solved in seven steps, which are described below in detail.

Step 1. Computation of the kernel. For each cell (numbered from 1 to M), we assign an elementary dipole in the three directions (x, y, z) (so three elementary dipoles in total) and we compute the resulting distributions of the potential at each of the N

recording electrodes. In each case, we remove the potential at the position of the selected reference electrode. Indeed, as explained in details in Jardani et al. (2008), the computed kernel should respect the potential at the selected reference electrode. The kernel is composed of three matrices $\mathbf{K} = [\mathbf{K}_x, \mathbf{K}_y, \mathbf{K}_z]$; each of these matrices $\mathbf{K}_i = (i = x, y, z)$ is an $N \times M$ matrix so $\mathbf{K}$ corresponds to an $N \times 3M$ matrix. The sources will be described by the current dipole moment vector $\mathbf{m} = i\mathbf{D}$, where $\mathbf{D}$ denotes the displacement vector pointing in the direction of the flow of the current (in the direction of the electric field) and $\mathbf{m}$ the current dipole moment vector (this is equivalent to the current density vector divided by the volume of the cell). The current dipole moment is therefore expressed in A m.

Step 2. The number of unknowns is $3M$ (three component for the current density times the number of cells). We have $3M \gg N$, the inverse problem is therefore strongly underdetermined. The inverse problem is solved with a gradient-based deterministic approach. The roles of data misfit and model objective functions are balanced using Tikhonov regularization (Tikhonov and Arsenin, 1977; Hansen, 1998; Jardani et al., 2008) through a global objective function, $P_\lambda(\mathbf{m})$, defined as

$$P_\lambda(\mathbf{m}) = \|\mathbf{d} - \mathbf{Km}\|_2 + \lambda s(\mathbf{m}), \tag{8}$$

where λ denotes a Lagrange regularization parameter ($0 < \lambda < \infty$) and $s(\mathbf{m})$ denotes the (stabilizing) regularizer. The vector $\mathbf{m}$ is the a vector composed of three vectors, one for each component (x, y, z): $\mathbf{m} = (\mathbf{m}_x, \mathbf{m}_y, \mathbf{m}_z)^T$ where the superscript T means transpose.

Step 3. The solution needs to be scaled with respect to the distance between the sources and the receivers. A depth weighting ($3M \times 3M$) diagonal matrix $\mathbf{J}$ can be computed from the kernel as

$$\mathbf{J} = \begin{bmatrix} \mathbf{J}_x & 0 & 0 \\ 0 & \mathbf{J}_y & 0 \\ 0 & 0 & \mathbf{J}_z \end{bmatrix}, \tag{9}$$

where each of the $\mathbf{J}_i (i = x, y, z)$ is a $(M \times M)$ diagonal matrix computed with

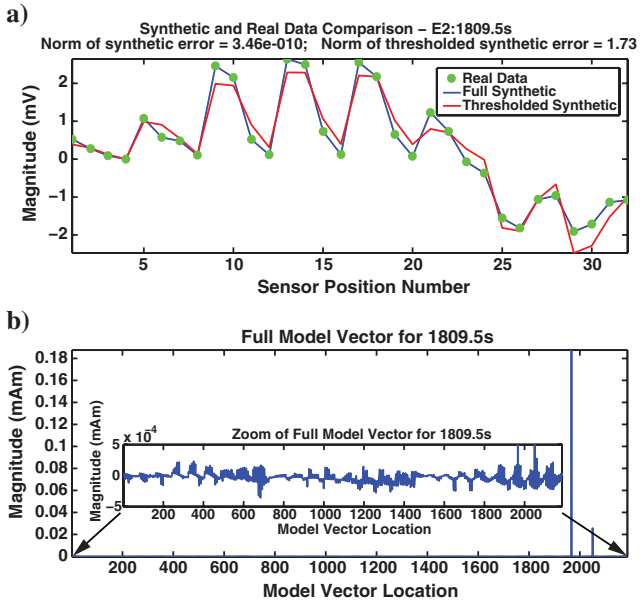

Figure 9. E2 compacted inversion results and forward modeled comparison with a thresholded forward model. (a) Comparison of the real data with the forward model calculations using the full inverted model, and a thresholded model derived from the full inversion model. (b) The full model vector that was found through inversion and compaction. The inset shows the multitude of minor dipoles spread throughout the model vector that were generated by the inversion and compaction process.

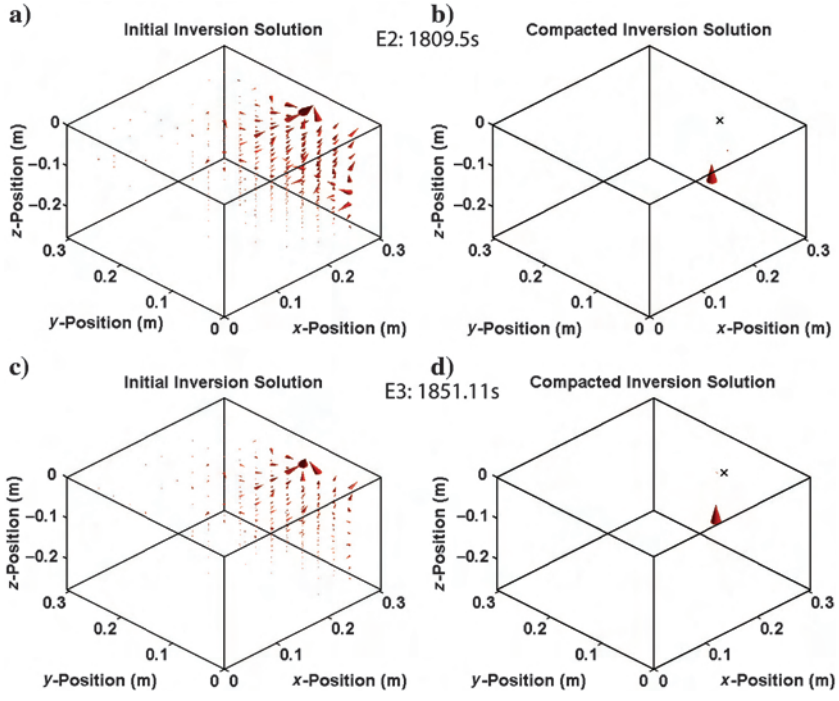

Figure 8. Initial and compacted dipole inversion results for events E2 and E3. In these cases, the compact inversion of events E2 and E3 yields one dipole that dominates the response through a higher magnitude. Note that event E3 is localized at a shallower depth than event E2, showing that the causative source is moving closer to the top surface of the block in the vicinity of hole #9. (a) Event E2 results of the source distribution after gradient-based inversion. (b) Same after 40 iterations in compacting the support of the source. (c and d) Same for event E3.

$$J_{ii}^{x,y,z} = \sum_{j=1}^{N} K_{ij}^{x,y,z}, \tag{10}$$

$$J_{ij}^{x,y,z}(i \neq j) = 0. \tag{11}$$

For compact source inversion, we seek to find one model with the minimum volume of the source current density. As shown by Last and Kubik (1983) and modified by Minsley et al. (2007) to incorporate depth weighting, the stabilizing functional is expressed as

$$\mathbf{\Omega} = \begin{bmatrix} \mathbf{\Omega}_x & 0 & 0 \\ 0 & \mathbf{\Omega}_y & 0 \\ 0 & 0 & \mathbf{\Omega}_z \end{bmatrix}, \tag{12}$$

where each of the $\mathbf{\Omega}_i (i = x, y, z)$ is an $(M \times M)$ diagonal matrix. The elements of these three matrices are

$$\Omega_{ii}^{x,y,z} = \sqrt{\frac{J_{ii}^{x,y,z}}{m_i^{x,y,z} + \beta^2}}, \tag{13}$$

$$\Omega_{ij}^{x,y,z}(i \neq j) = 0. \tag{14}$$

where β is a support parameter (our choice of β is explained further below). Zhdanov et al. (1994) show an efficient way to calculate the minimum support parameter β, whereas Minsley et al. (2007) discuss the role of multiple regularization parameters.

Step 4. We form the new normalized kernel matrix,

$$\mathbf{K}^* = [\mathbf{K}_x{}^*, \mathbf{K}_y{}^*, \mathbf{K}_z{}^*], \tag{15}$$

$$\mathbf{K}_{x,y,z}{}^* = \mathbf{K}_{x,y,z} \mathbf{\Omega}_{x,y,z}^{-1}, \tag{16}$$

where $\mathbf{K}^*$ is an $(N \times 3M)$ matrix.

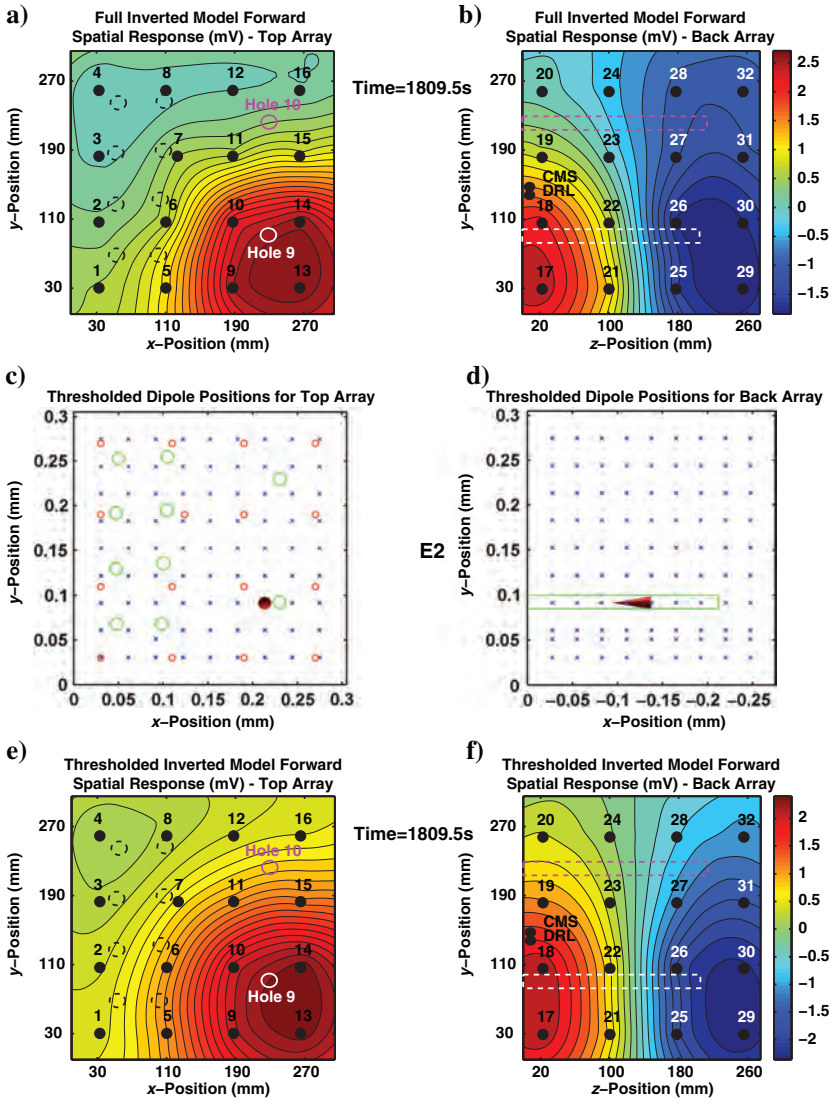

Figure 10. Spatial distributions and dipole location comparison for inverted and forward modeled results for event E2. (a and b) Forward computation results using the full model vector (all the minor dipoles included). (c and d) Thresholded model vector dipole positions (there are actually two dipoles in these panels) showing the orientation and position of the main dipole (visible). (e and f) Forward computation results using the thresholded model vector.

Step 5. We solve the following system of equations:

$$\begin{bmatrix} \mathbf{K}^* \\ \lambda \mathbf{I} \end{bmatrix} \mathbf{m}^* = \begin{bmatrix} \mathbf{d} \\ \mathbf{a} \end{bmatrix}, \tag{17}$$

where $\mathbf{I}$ is the $(3M \times 3M)$ identity matrix, $\mathbf{d}$ is the $(N \times 1)$ vector of electric potential data, $\mathbf{m}^*$ denotes the scaled $(3M \times 1)$ vector of model parameters, and $\mathbf{a}$ denotes a $(3M \times 1)$ vector with only zero.

Step 6. We need to unscale the solution to produce the $(3M \times 1)$ vector $\mathbf{m}$ obtained by

$$\mathbf{m} = [\mathbf{m}_x, \mathbf{m}_y, \mathbf{m}_z]^T \tag{18}$$

$$\mathbf{m}_{x,y,z} = \mathbf{\Omega}^{-1}_{x,y,z} \mathbf{m}_{x,y,z}{}^*. \tag{19}$$

The solution is found in terms of the current dipole moment expressed in A m. We use a small initial support parameter of $\beta = 10^{-12}$. Then for this value we compute the "best" value of the regularization parameter λ using the L-curve approach. If the solution is not compact enough, we multiply the previous value of β by 10 and repeat the process.

Step 7. The solution is thresholded to keep only the main dipoles that explain most of the solution. A threshold is applied to the model vector to remove all of the dipoles that were below the final value of β. The large number of low-magnitude dipoles that are generated by the gradient inversion process represent a purely mathematical solution to the source inversion. Therefore, it is considered that these small sources do not represent real sources and are not likely to be physically present during the event generation process. Thresholding these widely spread small dipoles removes the nonphysical, mathematical only contributions to the solution, allowing the comparison of the principal elements of the inversion with the real data. This helps to realistically quantify the inversion process and source localization error but does not affect the main components of the solution. Indeed, we expect the solution to be rather compact, and not broadly distributed. Thresholding does bias the solution; however, we expect the solution to be in the vicinity of hole #9 without components spread throughout the block volume.

The grid used for the previously described gradient-based approach combined with compactness is actually pretty coarse (see Figure 7). This is to reduce the computational effort and time to find a preliminary position for the source. As shown in the next section (see Figures 8–12), the inversion of the data leads to a source localized in the vicinity of hole #9 (as expected). Once this is done, we switch our inversion to the genetic algorithm on a refined grid located in the vicinity of the solution found by the gradient-based approach. The genetic algorithm used for this second inversion phase is described in the next section.

Inversion phase 2: Genetic algorithm approach

Following the gradient-based approach, we use a single dipole GA (genetic algorithm)-based search through a new and finer kernel matrix with 360 positions (Figure 13). This single dipole is assumed to represent the overall effect of pore water flow during the experiment. This assumption is expected to be good enough to locate the volume where the leak is occurring. The genetic algorithm is used as follows: a population of candidate solutions is used to find the solution of the inverse problem. This population has to evolve toward solutions that minimize the data misfit function,

$$P_d(\mathbf{m}) = \|\mathbf{d} - \mathbf{K}\mathbf{m}\|_2, \tag{20}$$

where $\|\cdot\|$ refers to the L2 norm. The evolution starts from the population of randomly generated individual solutions in the area found by the deterministic gradient-based algorithm described above. For each generation, the goodness of fit is evaluated through equation 20, and multiple individuals are stochastically selected from the current population and modified to form a new population. This new population is then used at the next iteration. The process is continued until a predetermined number of generations has been reached or a satisfactory data misfit has been reached for the population.

The model vector $\mathbf{m}$ contains $360 \times 3 = 1080$ elements (the number 3 represents the three components of the current dipole moment vector). The 360 positions of the kernel matrix are positioned on three concentric cylindrical surfaces centered around hole #9. Each cylindrical surface (radii = 0.0105, 0.0125, and 0.0145 mm) contains 10 z-axis levels with 4.4 mm spacing between levels, and 12 points in the x-y plane at each z-axis level equally spaced at 30° increments (see details in Figure 13). The kernel matrix was computed in the same way as the coarse kernel matrix, and resulted in a kernel matrix that was $(360 \times 3) \times 32$, or 1080×32 elements. The genetic algorithm we used is the one found in the MATLAB (Global optimization toolbox, Mathworks [R2012a], http://www.mathworks.com/products/global-optimization/, see function ga.m, and for additional details: http://www.mathworks.com/

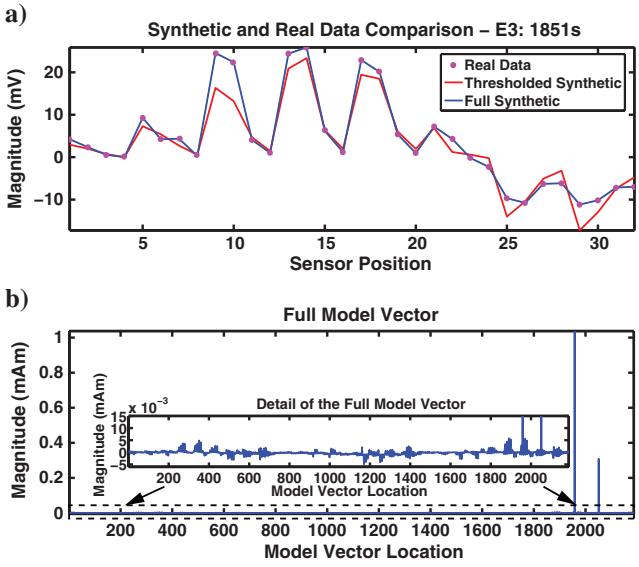

Figure 11. E3 compacted inversion results and forward modeled comparison with a thresholded forward model. (a) Comparison of the real data with the forward model calculations using the full inverted model, and a thresholded model derived from the full inversion model. (b) The full model vector that was found through inversion and compaction. The inset shows the multitude of minor dipoles spread throughout the model vector that were generated by the inversion and compaction process.

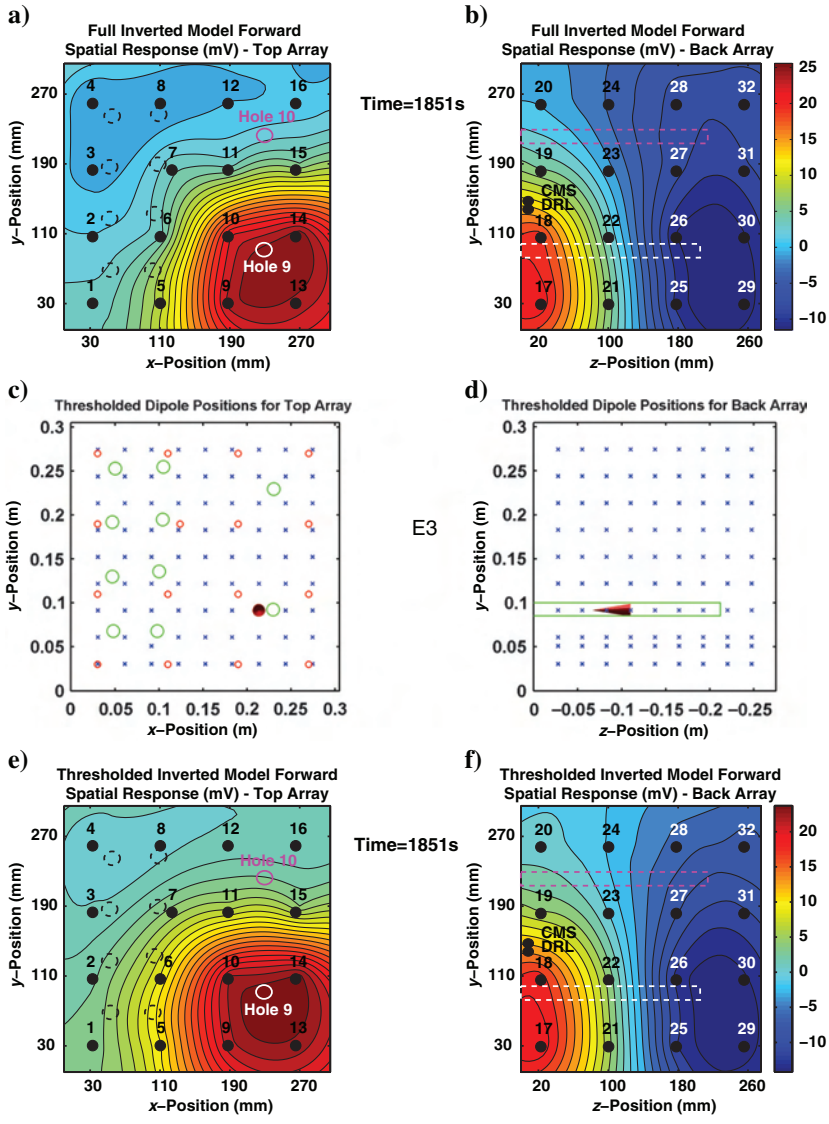

Figure 12. Spatial distributions and dipole location comparison for inverted and forward modeled results for event E3. (a and b) Forward computation results using the full model vector (all the minor dipoles included). (c and d) Thresholded model vector dipole positions (there are actually two dipoles in these panels) showing the orientation and position of the main dipole (visible). (e and f) Forward computation results using the thresholded model vector.

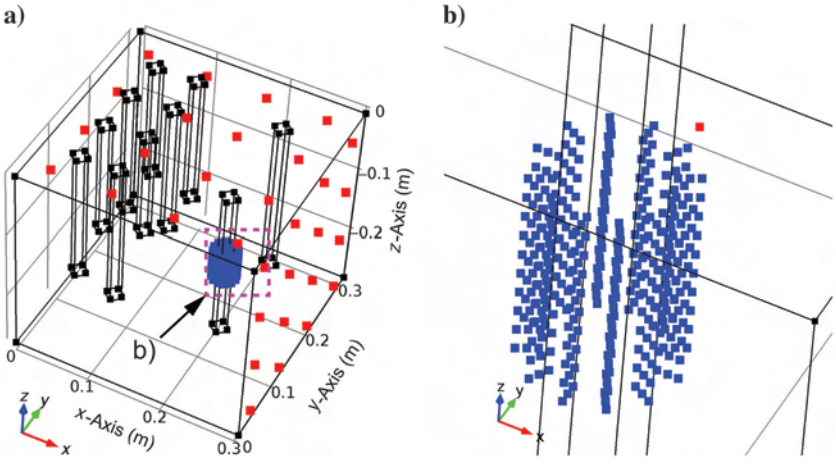

Figure 13. Comsol geometry used for the fine geometry kernel matrix computations (360 positions). (a) Finer resolution cylindrical kernel matrix point distribution along with the measurement points used with the genetic algorithm. (b) Close-up of the kernel matrix point distribution.

products/global-optimization/description4.html). It should be noted that Comsol Multiphysics renumbers the dipole points during its internal geometry point scan, and the dipole numbers listed here are aligned with this Comsol point sequence.

RESULTS OF THE INVERSION

Results of the gradient-based inversion

For phase 1 of the inversion, the model vector (2187×1 elements) represents the current dipole moment (magnitude in A m) at the 729 dipole positions in the model (at each location, the current dipole moment is characterized by three components along x, y, and z axes). The initial model vector solution of the gradient inversion process generates a large number of dipoles that are distributed throughout the volume of the model with dipole moments that are consistent with the electric potential distribution in the data. The compaction process changes the dipole moments, reducing the magnitude of most of the dipoles in the process. This results in a few (one or two) dominant dipoles with the rest of the points in the solution containing dipoles with very low magnitudes. Step 7 thresholds these small dipoles to make them equal to zero. Indeed, the large number of low magnitude dipoles represent a nonphysical mathematical solution to the inversion and therefore are not likely to be physically present during the event generation process that is expected to be quite localized.

To check how the thresholded solutions compares with the measured data, we look at the differences (using the L2 norm) between the respective model solutions and the real (measured) data. The forward modeled predictions of the data are called synthetic data below.

Figure 8 shows the comparison between the initial inversion results per one iteration (without compaction, Figure 8a and 8c) and the compacted solutions after 40 iterations (Figure 8b and 8d) for events E2 and E3, respectively. Each small cone in Figure 8 represents a dipole at a kernel matrix point, pointing in the direction of the electric current at that point. The compacted inversion (Figure 8b and 8d) results for both events shows a single dipole pointing mostly in the $+z$ direction. This solution is consistent with the hypothesis of seal leakage induced fluid flow based on the observations of the electric potential distribution (see Figure 5). Also the current is expected to occur in the direction of the fluid flow (via the drag of an excess of charge in the fluid-flow direction with a current flowing in the direction of the cations). Table 1 shows the L2 norm of the difference between the real data and the forward modeled full model vector (see equation 20, as well as the measured data and the forward modeled thresholded model vector). Table 2 shows the localization and dipole moment parameters for the events.

An in-depth analysis of event E2 is shown in Figures 9 and 10. Figure 9a shows that the forward-modeled full-model vector (with compaction and without thresholding) reproduces the real data nearly perfectly. Figure 9b shows the full-model-vector solution, and the inset shows the magnitude range for the minor dipoles. The thresholded model vector consists of only two dipoles (the rest of the thresholded model vector locations have negligible magnitudes) and is not shown here. It can be seen that the removal of all of the minor dipoles causes the L2 norm to increase substantially, making the thresholded model a poorer fit to the data. That said, the main characteristics of the data are preserved. Figure 10a and 10b shows the spatial voltage distribution generated by the full dipole model. These forward modeled results match extremely well with the kriged distribution of measured data shown in Figure 5a and 5b.

The use of compactness in the inversion focuses the dipole solutions at the kernel points that are the closest to hole #9 (Figure 10c and 10d). Figure 10e and 10f show the voltage spatial distribution that results from the forward modeled thresholded model vector. Comparing Figure 10e and 10f with Figure 10a and 10b shows some minor differences between the distributions. However, the main features are preserved. This indicates that the solution points generally to the correct location and direction near hole #9 for event E2.

The same analysis was carried out for event E3 (Figures 11 and 12). The fundamental results for event E2 apply to event E3 with a notable difference. The main dipole shown in Figure 12c is positioned at the same x-y location as the dipole responsible for event E2 in Figure 10c. However, the z-axis position of the main dipole shown in Figure 12d has moved up along hole #9. This is consistent with a hydromechanical disturbance related event moving upward along hole #9 over time. As discussed later, it is also consistent with the evolution of the position of the acoustic emissions over time.

Tables 1 and 2 summarize the coarse dipole matrix gradient inversion results. From these data it can be seen that the full-model inversion vectors produce excellent matches to the real data, but are not physical because we expect a localized source. The thresholded models get rid of the nonphysical dipoles, but yield, as expected, a

Table 1. Data rms error (L2 norm) comparison for events E2 and E3.

Event	Coarse kernel matrix model type	L2 norm	Number of dipoles
E2	Full model vector	3.46 e-10	729
E2	Thresholded model vector	1.73	2
E3	Full model vector	6.12 e-10	729
E3	Thresholded model vector	9.63	2

Table 2. Dipole locations from inverted coarse dipole point location matrix for events E2 and E3.

Event	Dipole status	Model vector #	Dipole #	x location (m)	y location (m)	z location (m)	Magnitude (mA m)	Direction
E2	Main dipole	1967	509	0.2135	0.0915	−0.1375	0.196	z-axis
E2	Minor dipole	2050	592	0.244	0.0915	−0.0825	0.017	z-axis
E3	Main dipole	1968	510	0.2135	0.0915	−0.11	1.56	z-axis
E3	Minor dipole	1332	603	0.244	0.122	−0.0825	−0.144	z-axis

solution that fits the data with a larger data rms error. This increase in rms error is expected because the coarse physical positions of the kernel matrix points used in this inversion do not perfectly match the true position of the source current density of the actual hydro-mechanical disturbance.

In conclusion, the result of the gradient-based inversion approach used in phase 1 provides reasonable estimation for the current dipole source locations at different times. We know from acoustic emissions (not shown here) and pressure data that there was no fracturing of the block during the experiment reported in this paper. Therefore all dipole solutions located far from hole #9 are considered not to have a physical cause, given that the current source is expected to be compact. The coarse nature of the inversion process calls for refinement, therefore this first set of solutions is used to direct the refinement of the source localization using the genetic algorithm.

Results of the genetic algorithm

Figure 14 shows the results of the genetic algorithm single dipole search for event E2. Figure 14a shows a plot of the data misfit error per equation 20 for each dipole position (the best solution is highlighted by the small red circle, dipole #42). This figure also shows how several other dipole positions come close to the minimum value of the data misfit error. These other points are at positions 11, 12, and 41. Because of the Comsol point sequence, these point positions represent spatially adjacent, or nearly adjacent positions.

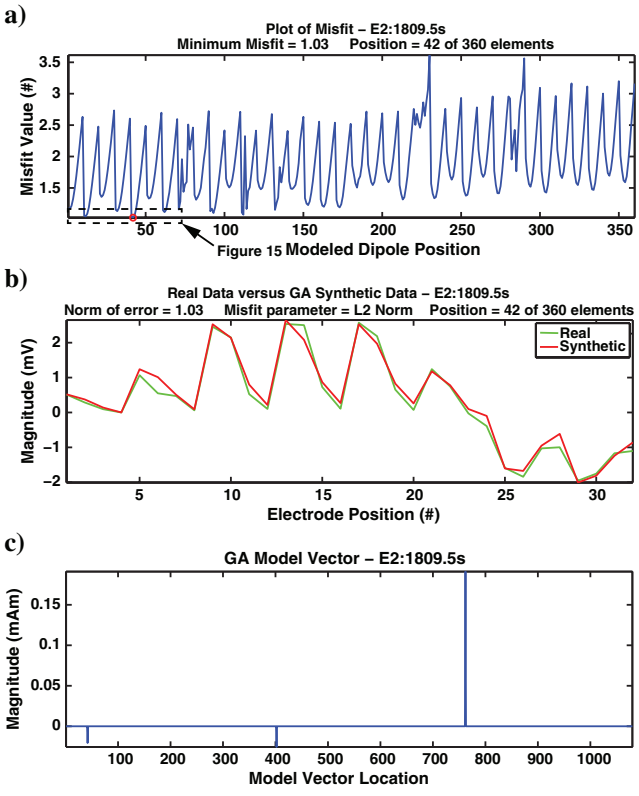

Figure 14. (a) The E2 related genetic algorithm localization misfit values for each position in the kernel matrix. The red circle represents the minimum value and therefore the best fit for the measured data, given the inversion constraints. (b) Comparison of the real data and the genetic algorithm based model vector forward computation. (c) The genetic algorithm based best fit model vector. Note that there are three points on the vector where there are values that are greater than zero. These points are exactly 360 elements apart, representing a single dipole moment orthogonal components.

Figure 14b shows the comparison of the real data with the forward model of the dipole that represents the minimum of the objective function. The synthetic data reproduces all of the major features of the real data with an improved L2 norm relative to the coarse gradient inversion results. The model vector for dipole #42 is shown in Figure 14c. Note the three positions that have nonzero values. These values represent the orthogonal components of the dipole moment found by the genetic algorithm. It can be seen that the dipole moment orients the dipole in a direction other than exactly along the z-axis of the block, which is slightly different from the results of the gradient inversion.

As shown in Figure 15, there are other dipoles that have objective function values that are close to the data misfit minimum obtained with dipole #42 (Figure 15). The black line in the figure represents the minimum of the data misfit error for comparison with other dipole position optimizations. This indicates that other solutions may yield equivalent or better results if more than one dipole is considered in the inversion process. Figure 16 shows the forward modeled results with dipole #42 only. The position of dipole #42 is located at 210° from the right side, on the second ring. The moment of the dipole (Figure 16e and 16f) generates a spatial distribution of the voltage that is tipped in a similar manner to the real data shown in Figure 5a and 5b. This orientation of the dipole implies that the axis of fluid flow is flowing mostly upward along the hole annulus with a slight flow direction away from the hole. This may be due to the way the epoxy is blocking the flow, causing a diversion of the flow away from hole #9.

Figure 17 shows the results of the genetic algorithm single dipole search for event E3. The black line in the figure represents the minimum of the data misfit error for comparison with other dipole position optimizations. The misfit for this event shows a minimum at position 47 (dipole #47) with a significant departure from the minimum as the dipole positions increase away from this position. Figure 18 shows that there are some other dipoles that have objective function values that are close to the data misfit minimum obtained with dipole #47, and are at positions 17, 18, 48, 77, and 78. This indicates that other solutions may yield equivalent or better results if more than one dipole is considered in the inversion process. Figure 19 shows the forward modeled results with dipole #47 only. The position of dipole #47 is located at 210° from the right side, on the second ring. The moment of the dipole (Figure 19e and 19f) generates a spatial distribution of the voltage that is tipped in a similar manner to the real data shown in Figure 5c and 5d. This orientation of the dipole implies that the axis of fluid flow is flowing mostly upward along the hole annulus with a slight flow direction away from the hole. This may be due to the way the epoxy is blocking the flow, causing a diversion of the flow away from hole #9. This GA-based inversion places the event E3 dipole higher than the dipole of event E2, with an orientation of the dipole moment that indicates the fluid flow axis is mostly upward along the hole with a slight tipping toward a tangent like trajectory along the hole. It should also be noted that dipole #47 is in a position that is directly above the dipole #42 position indicating that the flow between events E2 and E3 is likely to be mostly vertical. It should be

clarified here that the other impulses in the data may localize to different points along the hole, and may show other shifting of the flow pathway and therefore great care should be used to avoid overinterpreting the results of the inversion. Because of the relatively coarse resolution of this finer point spread, and the nonadjacency of the selected time slices, the subtleties of the fluid flow along the annulus of the hole cannot be resolved from this analysis. However, the dipole moments of these events may indicate unresolved fluid flow complexity.

Tables 3 and 4 summarize the genetic algorithm inversion results. Results with a fine grid dipole position matrix improves the localization, and helps to characterize the fluid flow directions that occurred during the seal failure. Comparing the dipole location data in Table 4 with those of Table 2 shows that the single dipole inversion using the genetic algorithm reproduces a similar degree of fit as the thresholded gradient inversion. Analysis of the position data from the two inversions show a high degree of consistency,

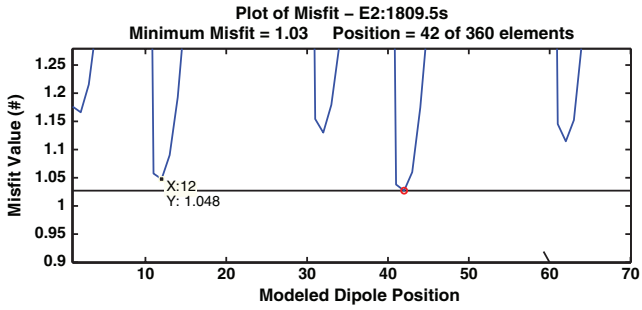

Figure 15. Zoomed in misfit for all the observations of the genetic search algorithm of event E2. This figure shows that there are dipole positions that are close to the minimum of the misfit function, which is shown by the small red circle. The position marked by $x = 12$ represents another possible location that is only slightly greater than the minimum found at 42. There are other points that are spatially adjacent to 42, including 11, and 41.

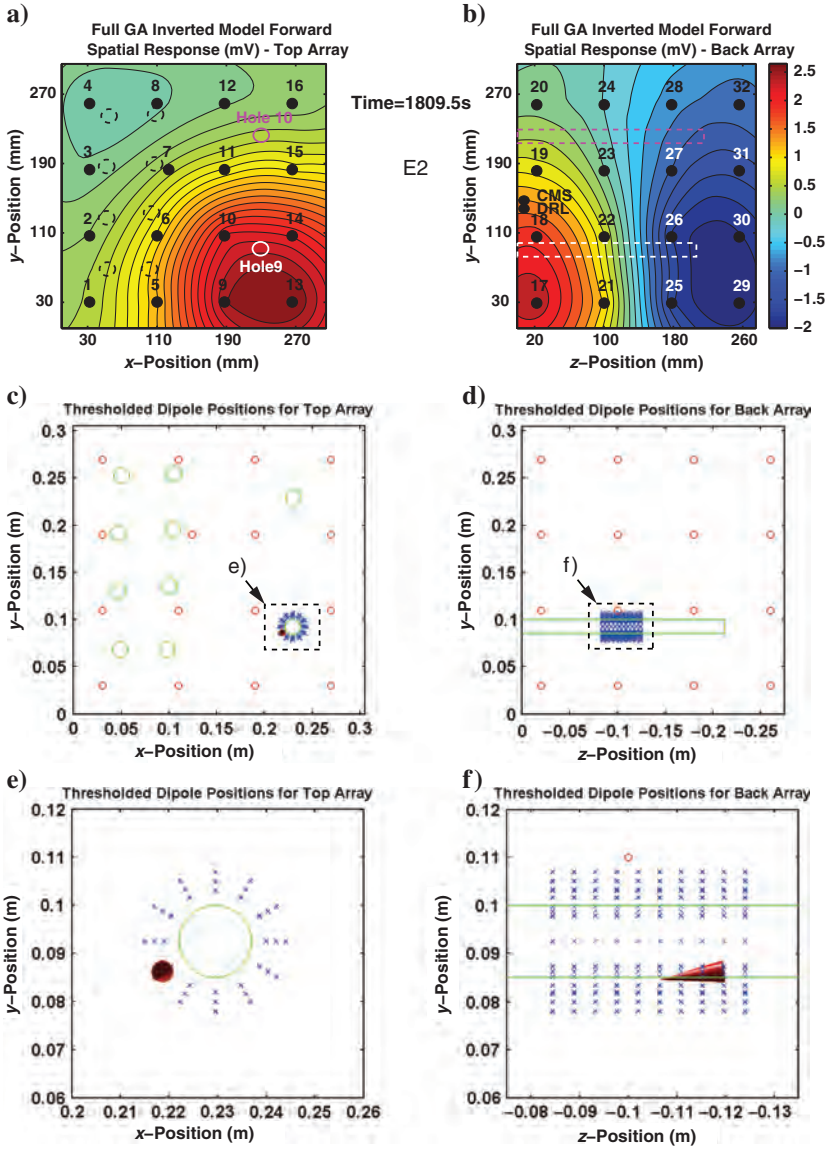

Figure 16. (a and b) Event E2 forward modeled voltage distribution of the genetic algorithm located dipole. (b and c) Spatial location of the dipole within the concrete block. (e and f) Close-up of the dipole location showing the off-vertical orientation of the dipole moment.

with all of the genetic algorithm located point coordinates falling inside the range of $\pm 1/2$ point spacing of the coarse dipole point matrix. This degree of location consistency is seen in the three columns on the right side of Table 5

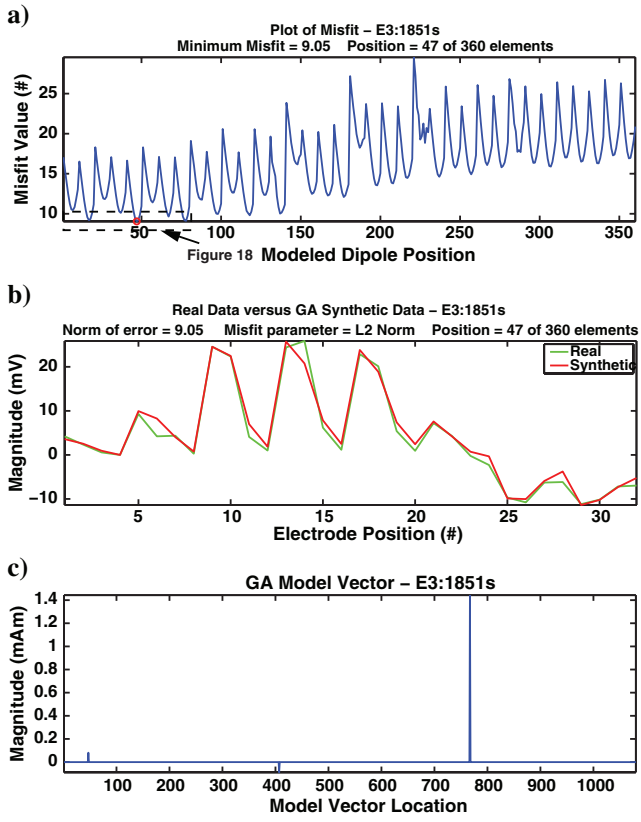

Figure 17. (a) E3 related genetic algorithm localization misfit values for each position in the kernel matrix. The red circle represents the minimum value and therefore the best fit for the measured data, given the inversion constraints. (b) Comparison of the real data and the genetic algorithm-based model vector forward computation. (c) The genetic-algorithm-based best fit model vector. Note that there are three points on the vector where there are values that are greater than zero. These points are exactly 360 elements apart, representing single dipole moment orthogonal components.

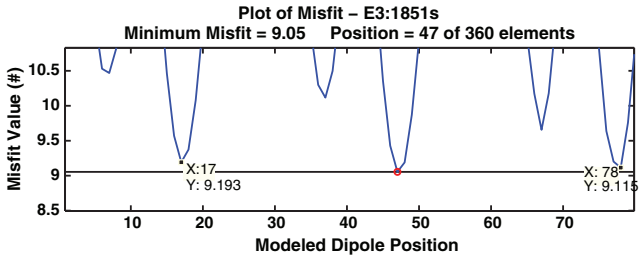

Figure 18. Zoom in the values of the misfit parameter obtained using the genetic-algorithm-based inversion of event E3. This figure shows that there are several dipole solutions that are close to the minimum of the data misfit function. In this figure, there are several other possible solutions, and they are all close to the point found at position 47, the minimum. These additional possible locations corresponds to dipole positions 17, 18, 48, 77, and 78.

Noise and position uncertainty analysis

A noise analysis was performed on the voltage and the pressure data sets, and the results show a very good S/N for both of these data sets. The base S/N for the pressure data was computed during the constant pressure phase of the experiment, before the pressure increases in the constant flow phase of the experiment. This portion of the signal had a mean pressure of 1169.8 kPa with an rms noise contribution of 1.4 kPa. This noise is what is used to compute the S/N of the pressure fluctuations that caused the leakage that was detected electrically. The smallest pressure change during an event was observed during the transition from the constant pressure period to the constant flow period (E0p) at time 1796 s (Figure 6). This event had a pressure increase of 13.3 kPa, resulting in an S/N of 9.8. All other events had higher S/Ns, ranging from about 22 at E3p to 108 at E5p. This results in the conclusion that all of the observed pressure changes were due to a physical change in the system and were not due to noise. Combined with the electric data, it is clear that the pressure changes were caused by seal breakage events that lead to a burst like fluid movement.

A noise analysis of the electric potential signals was also performed. The noise baseline was established after DC offset and trend removal, reference channel subtraction, and after the constant flow was initiated, but before the onset of rapid electric activity. Note that when the reference channel was subtracted, all residual correlated noises were removed, but the uncorrelated noise added in quadrature. This resulted in a net reduction of overall noise in all channels but channel 13 where the uncorrelated noise was dominant over the correlated noise component; the reference channel removal caused the noise in this channel to increase slightly. The mean rms noise level for all channels was computed, resulting in the observation that the noise level on channel 13 was more than nine times greater than the mean of the noise of all the other channels. The noise level on channel 13 is computed to be 0.121 mV rms, and the mean noise level of all channels (with the exception of channel 13) is 0.0134 mV rms. Inspection of the waveforms shown in Figure 3 shows clearly that the main events of interest have high voltage values relative to this calculated noise level. Because each channel represents a spatial measurement point on the cement block, only the channels that contribute to the peak voltage response are relevant to the S/N calculations. Events E2 and E3 have peak channel S/Ns of over 200 and over 1900, respectively. We conclude that the S/N of these channels does not contribute significantly to dipole location uncertainty.

Positional uncertainty analysis of the E2 GA current dipole solution was performed by adding Gaussian noise to the computed forward solution using the E2 dipole moment model vector. This new noisy measurement vector was used as the input to the genetic

Table 3. Genetic algorithm fit parameter comparison for events E2 and E3.

Event	Fine kernel matrix model type	L2 norm	Number of dipoles
E2	Single dipole model vector	1.03	1
E3	Single dipole model vector	9.05	1

algorithm, where a new dipole solution would be computed. The new solution would be compared with the initial solution. Three levels of noise were used in this analysis, 1%, 5%, and 10% noise levels were used. These noise levels were computed at as a random Gaussian additive voltage computed from the mean voltage of each channel. Solutions for the three noise cases were found at the following dipole point positions: 2 for 1%, 62 for 5%, and 61 for 10% noise. These solution points have a displacement from the initial solution of one radial dipole point in the position from the initial solution point in the matrix. The new point solutions are generally biased in the positive y-direction (see Figure 20). The results of this noise analysis demonstrates the robustness of the solution method by showing the volumetric clustering nature of all of the solutions in the same general area. The bias in the computed noise solutions may indicate that the true solution for the problem resides somewhere in between the initial solution and the noise-based solutions. The coarse nature of the point matrix forces solutions that are on the point matrix grid, and therefore this is a significant contribution to the degree of error in the solution misfit, as well as the simple dipole approximation assumption.

Table 4. Genetic algorithm inverted dipole locations for events E2 and E3.

Event	Model vector #	Dipole #	x location (m)	y location (m)	z location (m)	Moment x (A m)	Moment y (A m)	Moment z (A m)
E2	42	42	0.2187	0.08625	−0.1196	−0.0207	−0.0256	0.1910
E3	47	47	0.2187	0.08625	−0.0976	0.08104	−0.0884	1.4433

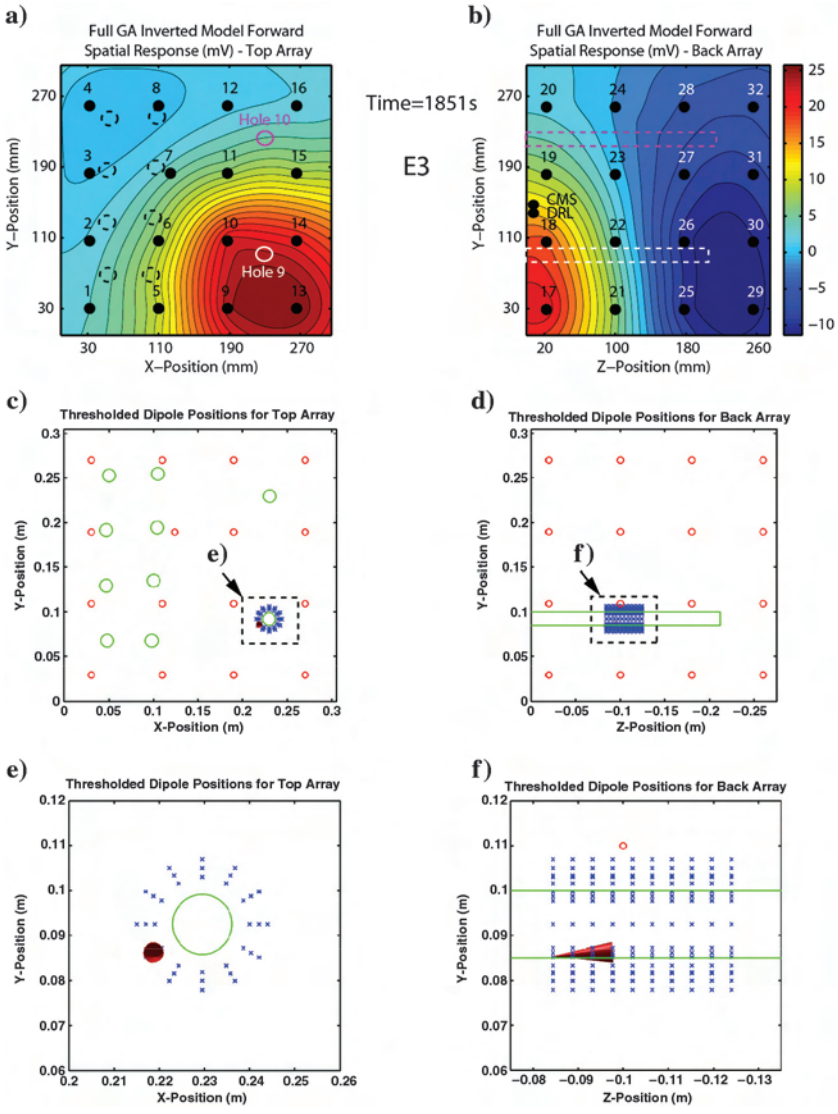

Figure 19. Localization of the causative source of current. (a and b) E3 forward modeled voltage distribution of the genetic algorithm located dipole. (b and c) Spatial location of the dipole within the concrete block. (e and f) Close-up of the dipole location showing the vertical orientation of the dipole moment.

DISCUSSION

Comparison with the acoustic emissions

The acoustic emission hit count data (see Figure 6a) indicates nominally progressive increases in breakage intensity around the times of the pressure changes. The localization of the acoustic emissions is shown in Figure 21. Some of the acoustic emission hits are due to activity far from hole #9. These acoustic emission hits could be associated with stress changes and the reactivation of existing fractures in the block. Indeed because the block is unconfined, there may be numerous surface events that would be generated by the cracking of the block surface as it expands under increased internal fluid pressure. This type of event is highly localizable because it is associated with clear arrivals in the acoustic emissions.

The events associated with the seal rupture along hole #9 are difficult to localize for two reasons: (1) there are too many overlapping events to localize them; (2) some events have likely a tremor type signature which makes localization difficult. It seems however that several events localized close to hole #9 progresses further up over

Table 5. Dipole position changes for E2 and E3 for coarse and fine point locations.

Event	Model vector #	Dipole #	x location (m)	y location (m)	z location (m)	x difference (m)	y difference (m)	z difference (m)
E2 (1)	1967	509	0.2135	0.0915	−0.1375	$\Delta x/2 = 0.01525$		
E3 (1)	1968	510	0.2135	0.0915	−0.11	$\Delta y/2 = 0.01525$	$\Delta z/2 = 0.01375$	
E2 (2)	42	42	0.2187	0.08625	−0.1196	0.00517	−0.00525	0.0179
E3 (2)	47	47	0.2187	0.08625	−0.0976	0.00517	−0.00525	0.0124

(1) Coarse dipole matrix
(2) Fine dipole matrix

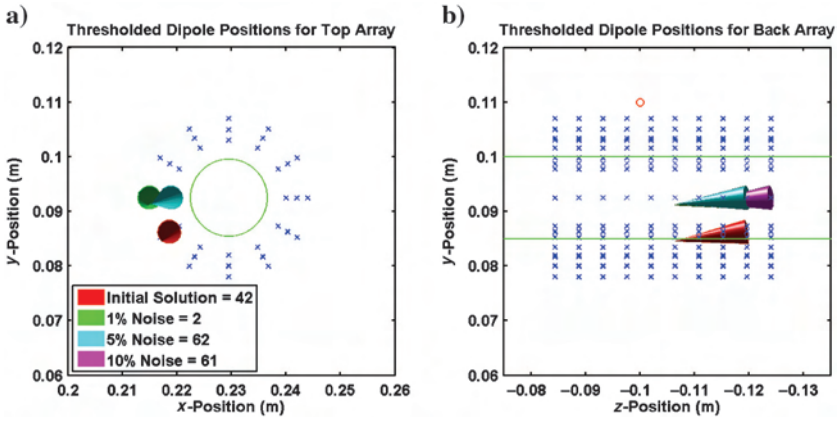

Figure 20. Localization of the causative source of current and noise analysis. (a and b) These figures show the spatial positions of the dipoles found during the localization uncertainty test. Note that the solutions cluster near the initial solution found during the inversion process. The bias in the $+y$- and $-z$-directions may indicate that the true solution may be between the solutions with noisy data and the solution found initially.

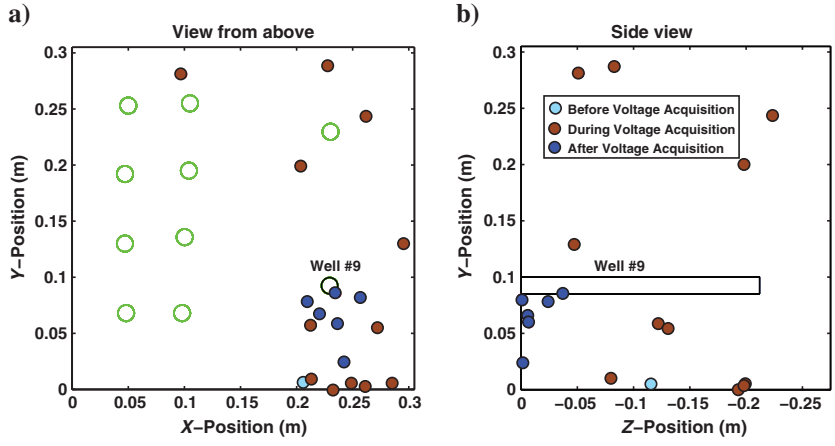

Figure 21. Localization of the acoustic emissions with respect to the time window shown in Figure 6. The events localized far from hole #9 are probably associated with the reactivation of small cracks. Note that only a tiny fraction of the AE hits shown in Figure 6 are localizable.

time along the well in agreement with the localization of the source current density associated with the burst in the electric field. Note that the latest AE localizations occur near the top of the injection well at the time where the seal failure was confirmed through the appearance of water on the surface of the block and indicate surface breakthrough. This is showing the possibility in the future to perform a joint localization of the electric and acoustic emission data to improve the localization of the hydromechanical disturbances.

Nature of the coupling mechanism

The second point to address concerns the nature of the coupling mechanism. We define the sensitivity coefficient of the voltage with respect to the fluid pressure changes as

$$C = \left(\frac{\partial \varphi}{\partial p}\right)_{j=0}. \tag{21}$$

When the coupling process is electrokinetic in nature (i.e., related to a relative displacement between the solid skeleton and the pore water), the coupling coefficient scales with the pore-water conductivity (e.g., Revil et al., 2003). In the present case, the coupling coefficient is roughly estimated to be on the order of -20 mV MPa^{-1} from the data shown in Figure 6b and 6c (typically, 3–6 mV variations for 0.2–0.3 MPa of pore fluid pressure changes) at a pore-water conductivity of 1.7 S m^{-1}. In Figure 22, we plotted the data of Revil et al. (2003) with the result of the present estimate (roughly -20 mV MPa^{-1}). The present estimate of the coupling coefficient matches the trend for electrokinetic data implying that the mechanism we observed is likely to be electrokinetic in nature.

Potential applications

The results presented here have several applications. In the oil and gas industry, the extension of these laboratory observations to field applications can help close the knowledge gap associated with the risks of drilling, completion, and hydraulic fracturing

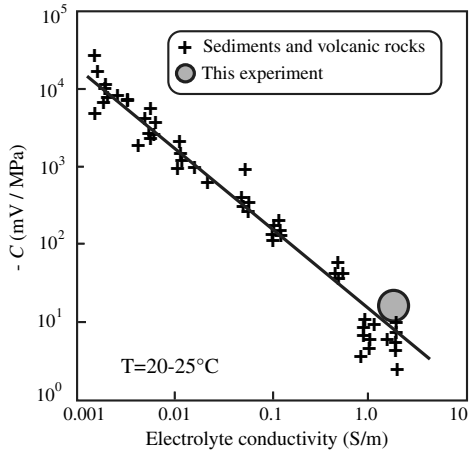

Figure 22. Comparison between the coupling coefficient inferred from the block experiment (this study) and the experimentally measured streaming potential coupling coefficients reported by Revil et al. (2003). The consistency between the data indicates that the observed coupling mechanism is likely to be electrokinetic in nature.

operations. This can be accomplished by electrically monitoring drinking water aquifers with an aquifer safety system designed to detect undesirable leaks of fluids or gases in their very early stages, before damage can occur. This type of system would be able to detect and localize annulus flow of fluids upward in the well system, or the displacement of fluids by gases. In older oil and gas wells, it may be possible to assess the presence of microannulus and its connectivity to protected aquifer formations. For old, reentrant oil and gas fields, old plugged and abandoned wells may be assessed for integrity and microannulus issues associated with protected aquifer formations. Additionally, it may be possible to monitor aquifer systems for potential long-term problems by employing continuous aquifer monitoring based on the physical principals and some of the measurement concepts used for these experiments.

These results also indicate that fluid flowing in the annulus of the well (in contact with porous media such as concrete, or natural formations) and can be somehow connected to pore water flowing in a network of cracks. As such, this pore water flow would produce electric signals similar to those observed in these experiments. This could lead to the ability to help characterize fractured rock systems through the movement of the fluids within them. This opens up a new area of fractured rock characterization through passive electric potential measurement, and may lead to the characterization of the fracture networks that open up in hydraulically fractured formations.

This also indicates that methods based on these results can be used for carbon sequestration monitoring, or the assessment of the integrity of existing wells for use in carbon sequestration applications. Displacement of existing, natural fluids by escaping carbon dioxide is likely to generate an electric response that can be detected using electrical potential based measurement techniques. Early indication of well integrity problems that allow carbon dioxide upward migration will greatly facilitate carbon sequestration system repair, enhancing carbon sequestration system reliability. Several very near surface civil and environmental applications could also benefit from the findings presented here. For example, injection grouting is commonly used to fill voids in soil and rock, strengthen weak soil, and slow water seepage, e.g., in dams and levees. One significant limitation in current practice is the inability to track the movement of grout during injection. Passive electric potential measurements could be employed to address this challenge. Further, environmental applications involve tracking fluid flow associated with injection and pumping gallery remediation techniques. Passive electric potential measurements could be used to check for biofouling of the screens or ports on the relevant wells or other relevant changes to the flow field. This can improve system efficiency by detecting reduction in flow rates or changes in the flow pattern through ports in gallery wells or within the formation. It is also possible to apply these techniques to water wells of a diverse variety to check for a variety of situations such as determining the source or direction of the water, fouling or failure of water uptake or injection systems, and other issues related to well integrity.

CONCLUSIONS

Two important observations have come from the experimental data. First, borehole seal failure during hydraulic fracturing generated electric current densities and measurable electric potentials when fracturing fluid flowed into the annulus between the hole wall and the casing and came in contact with the borehole wall. Second, we have shown that the source current density associated with the

seal leak can be located using a self-potential tomography technique. From these data, the concept of detecting nonintrusively well system leakages can be developed.

Further work with these data will be to combine the electric data with the acquired pressure, and acoustic emission data (different data acquisition systems) and perform a fully integrated analysis. An additional follow-on step will be to perform a 4D inversion using temporal regularization to develop a temporal fluid flow history of the leakage. A possibility could be to use the active time constrained approach for that purpose. We plan also to develop field scale experiments at various scales (from few meters to several kilometers) to check how this approach can be applied in field conditions.

ACKNOWLEDGMENTS

We thank NSF for funding the SmartGeo Educational Program (Project IGERT: Intelligent Geosystems; DGE-0801692) as well as the U. S. Department of Energy (Geothermal Technology Advancement for Rapid Development of Resources in the U. S., GEODE, award #DE-EE0005513 to A. Revil as well as award DE-FE0002760 to M. Guttierez), the Petroleum Institute of Abu Dhabi, and the Coupled Integrated Multiscale Measurements and Modeling (CIMMM) consortium in Unconventional Gas Shale and Shale Oil Reservoirs at Mines. The opinions expressed in this paper are those of the authors and not the DOE and NSF. We thank Terry Young for his support at Mines.

REFERENCES

Agarwal, R. G., R. D. Carter, and C. B. Pollock, 1979, Amoco evaluation and performance prediction of low-permeability gas wells stimulated by massive hydraulic fracturing: Journal of Petroleum Technology, **31**, 362–372.

Ansari-Asl, K., G. Chanel, and T. Pun, 2007, Channel selection method for EEG classification in emotion assessment based on synchronisation likehood: 15th European Signal Processing Conference (EUSIPCO 2007), EURASIP, 1241–1245.

Bolève, A., A. Crespy, A. Revil, F. Janod, and J. L. Mattiuzzo, 2007, Streaming potentials of granular media: Influence of the Dukhin and Reynolds numbers: Journal of Geophysical Research, **112**, B08204, doi: 10.1029/2006JB004673.

Byrdina, S., S. Friedel, J. Wassermann, and J. Zlotnicki, 2003, Self-potential variations associated with ultra-long period seismic signals at Merapi volcano: Geophysical Research Letters, **30**, 2156, doi: 10.1029/2003GL018272.

Castermant, J., C. A. Mendonça, A. Revil, F. Trolard, G. Bourrié, and N. Linde, 2008, Redox potential distribution inferred from self-potential measurements associated with the corrosion of a burden metallic body: Geophysical Prospecting, **56**, 269–282.

Chen, M. Y., B. Raghuraman, I. Bryant, M. G. Supp, and J. Navarro, 2005, Wireline apparatus for measuring streaming potentials and determining earth formation characteristics: U. S. Patent 6,978,672.

Chen, M. Y., B. Raghuraman, I. Bryant, M. G. Supp, and J. Navarro, 2007, Methods for locating formation fractures and monitoring well completion using streaming potential transients information: U. S. Patent 7,243,718.

Chen, M. Y., B. Raghuraman, I. Bryant, M. G. Supp, and J. Navarro, 2011, Completion apparatus for measuring streaming potentials and determining earth formation characteristics: U. S. Patent 7,891,417.

Chen, S., and E. Wang, 2011, Electromagnetic radiation signals of coal or rock denoising based on morphological filter: Procedia Engineering, **26**, 588–594, doi: 10.1016/j.proeng.2011.11.2210.

Cihan, A., Q. Zhou, and J. T. Birkholzer, 2011, Analytical solutions for pressure perturbation and fluid leakage through aquitards and wells in multilayered-aquifer systems: Water Resources Research, **47**, W10504, doi: 10.1029/2011WR010721.

Crespy, A., A. Revil, N. Linde, S. Byrdina, A. Jardani, A. Bolève, and P. Henry, 2008, Detection and localization of hydromechanical disturbances in a sandbox using the self-potential method: Journal of Geophysical Research, **113**, B01205, doi: 10.1029/2007JB005042.

Duru, A. D., A. Ademoglu, and T. Demiralp, 2009, Analysis of brain electrical topography by spatio-temporal wavelet decomposition: Mathematical and Computer Modelling, **49**, 2224–2235.

Entov, V. M., Y. N. Gordeev, E. M. Chekhonin, and M. J. Thiercelin, 2010, Method and an apparatus for evaluating a geometry of a hydraulic fracture in a rock formation: U. S. Patent 7,819,181.

Frash, L. P., and M. Gutierrez, 2012, Development of a new temperature controlled true-triaxial apparatus for simulating enhanced geothermal systems (EGS) at the laboratory scale: Proc. 37th Workshop on Geothermal Reservoir Engineering, Stanford University, SGP-TR-194.

Grech, R., T. Cassar, J. Muscat, K. P. Camilleri, S. G. Fabri, M. Zervakis, P. Xanthopoulos, V. Sakkalis, and B. Vanrumste, 2008, Review on solving the inverse problem in EEG source analysis: Journal of NeuroEngineering and Rehabilitation, **5**, no. 25, 1–33, doi: 10.1186/1743-0003-5-25.

Haas, A., and A. Revil, 2009, Electrical signature of pore scale displacements: Water Resources Research, **45**, W10202, doi: 10.1029/2009WR008160.

Hampton, J., 2012, Laboratory hydraulic fracture characterization using acoustic emission: M.S. thesis, Colorado School of Mines.

Hansen, P. C., 1998, Rank-deficient and discrete ill-posed problems: Numerical aspects of linear inversion: SIAM.

He, X., W. Chen, B. Nie, and H. Mitri, 2011, Electromagnetic emission theory and its application to dynamic phenomena in coal-rock: International Journal of Rock Mechanics and Mining Sciences, **48**, 1352–1358, doi: 10.1016/j.ijrmms.2011.09.004.

He, X., B. Nie, W. Chen, E. Wang, L. Dou, Y. Wang, M. Liu, and M. Hani, 2012, Research progress on electromagnetic radiation in gas-containing coal and rock fracture and its applications: Safety Science, **50**, 728–735.

Ikard, S. J., A. Revil, A. Jardani, W. F. Woodruff, M. Parekh, and M. Mooney, 2012, Saline pulse test monitoring with the self-potential method to non-intrusively determine the velocity of the pore water in leaking areas of earth dams and embankments: Water Resources Research, **48**, W04201, doi: 10.1029/2010WR010247.

Jardani, A., A. Revil, A. Bolève, and J. P. Dupont, 2008, 3D inversion of self-potential data used to constrain the pattern of ground water flow in geothermal fields: Journal of Geophysical Research, **113**, B09204, doi: 10.1029/2007JB005302.

Jia, H., E. Wang, X. Song, H. Zhang, and Z. Li, 2009, Correlation of electromagnetic radiation emitted from coal or rock to supporting resistance: Mining Science and Technology (China), **19**, no. 3, 317–320, doi: 10.1016/S1674-5264(09)60059-4.

Kappenman, E. S., and S. J. Luck, 2010, The effects of electrode impedance on data quality and statistical significance in ERP recordings: Psychophysiology, **47**, no. 5, 888–904, doi: 10.1111/j.1469-8986.2010.01009.x.

Karaoulis, M., J.-H. Kim, and P. I. Tsourlos, 2011a, 4D active time constrained inversion: Journal of Applied Geophysics, **73**, 25–34.

Karaoulis, M., A. Revil, D. D. Werkema, B. Minsley, W. F. Woodruff, and A. Kemna, 2011b, Time-lapse 3D inversion of complex conductivity data using an active time constrained (ATC) approach: Geophysical Journal International, **187**, 237–251, doi: 10.1111/j.1365-246X.2011.05156.x.

Keck, R. G., and R. J. Withers, 1979, A field demonstration of hydraulic fracturing for solids waste injection with real-time passive seismic monitoring: SPE Annual Technical Conference and Exhibition, doi: 10.2118/28495-MS.

Kohl, T., K. F. Evansi, R. J. Hopkirk, and L. Rybach, 1995, Coupled hydraulic, thermal and mechanical considerations for the simulation of hot dry rock reservoirs: Geothermics, **24**, no. 3, 345–359.

Kuriyagawa, M., H. Kobayashi, I. Matsunaga, T. Yamaguchi, and K. Hibiya, 1989, Application of hydraulic fracturing to three-dimensional in situ stress measurement: International Journal of Rock Mechanics and Mining Sciences and Geomechanics Abstracts, **26**, no. 6, 587–593.

Kuznetsov, V. V., V. V. Plotkin, S. Y. Khomutov, O. M. Grekhov, A. F. Pavlov, and A. N. Fedorov, 2001, Powerful seismovibrators as a possible source of acoustic and electromagnetic disturbances: Physics and Chemistry of the Earth, Part A: Solid Earth and Geodesy, **25**, no. 3, 325–328, doi: 10.1016/S1464-1895(00)00051-X.

Last, B. J., and K. Kubik, 1983, Compact gravity inversion: Geophysics, **48**, 713–721, doi: 10.1190/1.1441501.

Lee, J. S., C. S. Bang, and I.-Y. Choi, 1999, Analysis of borehole instability due to grouting pressure: 37th U.S. Symposium on Rock Mechanics (USRMS).

Mahardika, H., A. Revil, and A. Jardani, 2012, Waveform joint inversion of seismograms and electrograms for moment tensor characterization of fracking events: Geophysics, **77**, no. 5, ID23–ID39, doi: 10.1190/GEO2012-0019.1.

Mendonça, C. A., 2008, Forward and inverse self-potential modeling in mineral exploration: Geophysics, **73**, no. 1, F33–F43, doi: 10.1190/1.2821191.

Minsley, B. J., J. Sogade, and F. D. Morgan, 2007, Three-dimensional source inversion of self-potential data: Journal of Geophysical Research, **112**, B02202, doi: 10.1029/2006JB004262.

Moore, J. R., and S. D. Glaser, 2007, Self-potential observations during hydraulic fracturing: Journal of Geophysical Research, **112**, B02204, doi: 10.1029/2006JB004373. 23.

Nie, B., X. He, and C. Zhu, 2009, Study on mechanical property and electromagnetic emission during the fracture process of combined coal-rock: Procedia Earth and Planetary Science, **1**, no. 1, 281–287.

Onuma, K., J. Muto, H. Nagahama, and K. Otsuki, 2011, Electric potential changes associated with nucleation of stick-slip of simulated gouges: Tectonophysics, **502**, no. 3–4, 308–314.

Revil, A., and N. Linde, 2006, Chemico-electromechanical coupling in microporous media: Journal of Colloid and Interface Science, **302**, 682–694.

Revil, A., C. A. Mendonça, E. Atekwana, B. Kulessa, S. S. Hubbard, and K. Bolhen, 2010, Understanding biogeobatteries: Where geophysics meets microbiology: Journal of Geophysical Research, **115**, G00G02, doi: 10.1029/2009JG001065.

Revil, A., V. Naudet, J. Nouzaret, and M. Pessel, 2003, Principles of electrography applied to self-potential electrokinetic sources and hydrogeological applications: Water Resources Research, **39**, no. 5, 1114, doi: 10.1029/2001WR000916.

Revil, A., W. F. Woodruff, and N. Lu, 2011, Constitutive equations for coupled flows in clay materials: Water Resources Research, **47**, W05548, doi: 10.1029/2010WR010002.

Sato, M., and H. M. Mooney, 1960, The electrochemical mechanism of sulfide self-potentials: Geophysics, **25**, 226–249, doi: 10.1190/1.1438689.

Tikhonov, A. N., and V. Y. Arsenin, 1977, Solutions of ill-posed problems: John Wiley & Sons.

Ushijima, K., H. Mizunaga, and T. Tanaka, 1999, Reservoir monitoring by a 4-D electrical technique: The Leading Edge, **12**, 1422–1424.

Wang, E., X. He, J. Wei, B. Nie, and D. Song, 2011, Electromagnetic emission graded warning model and its applications against coal rock dynamic collapses: International Journal of Rock Mechanics and Mining Sciences, **48**, no. 4, 556–564, doi: 10.1016/j.ijrmms.2011.02.006.

Warpinski, N. R., 1991, Hydraulic fracturing in tight, fissured media: Journal of Petroleum Technology, **43**, no. 2, 146–151, 208–209.

Wishart, D. N., L. Slater, D. L. Schnell, and G. C. Herman, 2008, Hydraulic anisotropy characterization of pneumatic-fractured sediments using self-potential gradient: Journal of Contaminant Hydrology, **103**, 133–144.

Wurmstich, B., and F. D. Morgan, 1994, Modeling of streaming potential responses caused by oil well pumping: Geophysics, **59**, 46–56, doi: 10.1190/1.1443533.

Zhdanov, A., 1994, Direct recurrence algorithms for solving the linear equations of the method of least-squares: Computational Mathematics and Mathematical Physics, **34**, 693–701.